Computer Methods in Applied Mechanics and Engineering 449 (2026) 118446

Contents lists available at ScienceDirect

Comput. Methods Appl. Mech. Engrg.

journal homepage: www.elsevier.com/locate/cma

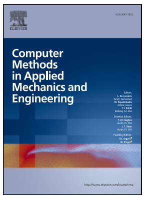

Topology optimization for pressure-dependent elastoplastic structures considering a smooth hyperbolic approximation of the Drucker-Prager yield criterion

Emily Alcazar, Glaucio H. Paulino *

Department of Civil and Environmental Engineering, Princeton University, Princeton, NJ, 08544, USA

ARTICLE INFO

Keywords:
Drucker-prager
Pressure-dependent elastoplasticity
Topology optimization
Smooth approximation

ABSTRACT

A topology optimization framework considering a smooth hyperbolic Drucker-Prager (SHDP) plasticity is presented. The smooth hyperbolic approximation is used to address the gradient-discontinuity of the Drucker-Prager yield surface at the apex, for accurate sensitivity information and improved numerical stability for both the stress integration scheme and the optimization sensitivity analysis. The return mapping algorithm for this constitutive model, based on two stress invariants, is derived and presented herein along with a discussion on the update of the plastic multiplier increment through the bisection method. In this work, pressure-dependent elastoplastic structures with high energy absorption are designed through an objective function of maximizing plastic work. The pressure-dependence of metal plasticity motivates the use of the smooth hyperbolic Drucker-Prager to model metal alloys. The path dependent sensitivity analysis was conducted using the adjoint method with all the partial derivatives computed analytically. The effectiveness of the proposed framework is demonstrated by the numerical results, where the structures significantly differ from those based on only the deviatoric stress invariant in the elasto-plastic model. Lastly, we demonstrate that the proposed regularized SHDP framework allows for convergence in the forward analysis and subsequently the topology optimization problem in cases where the original Drucker-Prager could not.

1. Introduction

Topology optimization is a powerful engineering technique which determines an optimal material layout for a given design domain to enhance a specified objective. Since its inception in 1988 [1], topology optimization has made significant progress in many areas; however, most of the work in the literature is constrained either to linear or nonlinear elasticity [2,3]. In this work, we aim to add to the existing literature of topology optimization considering elastoplasticity [4–8]. Hence we incorporate the energy dissipative phenomenon and history-dependent deformation, as found in real-life materials, into the topology optimization framework.

Von Mises made a seminal contribution in the field of mechanics by deriving the complete set of equations of motion required to model plastically-deformable bodies [9]. Since then the von Mises yield criterion is still widely used today and is the most dominant constitutive model used in elastoplastic topology optimization frameworks [10–17]. The von Mises yield criterion models the material behavior of metals where plastic yielding is described to occur when the J_2 stress invariant reaches a critical value. The claim that standard metal plasticity is independent of hydrostatic stress has been corroborated in experimental studies [18] and is still

---

* Corresponding author.
E-mail addresses: ea2385@princeton.edu (E. Alcazar), gpaulino@princeton.edu (G.H. Paulino).

https://doi.org/10.1016/j.cma.2025.118446
Received 16 April 2025; Received in revised form 5 September 2025; Accepted 29 September 2025

widely assumed to be true in current works of metal plasticity [19,20]. However, in recent decades, this postulate has come under reexamination with experimental data supporting the argument that metals experience yielding effects under certain hydrostatic pressure levels. This was demonstrated in the work by Spitzig et al. [21] where they conducted tension and compression tests under hydrostatic pressure on steel specimens which indicated a linear relationship between the yield strength and the hydrostatic pressure - equivalent to the yield criterion by Drucker and Prager [22] initially proposed for the material characterization of soil and other granular geomaterials. Later, Wilson [23] obtained experimental data from aluminum alloy specimens in conjunction with numerical simulations to demonstrate the accuracy of the Drucker-Prager yield criterion in capturing the effects of hydrostatic tensile stress on yielding. These experiments provide additional evidence in motivating the inclusion of pressure in the yield criterion for metal plasticity. Additional work by Bai and Wierzbicki [24] argue the inclusion of the three stress invariants, through experimental results, in a proposed yield criterion to better represent metal plasticity. However, for the sake of this work, we use the yield criterion dependent on two stress invariants.

For non-smooth yield functions, there exist gradient-discontinuities which may cause instabilities and computational difficulties in stress integration schemes leading to inefficiency or potentially failure overall. Thus the treatment of these singularities has been extensively studied, such as in the work by Abbo and Sloan [25], where the non-smoothness of the Mohr-Coulomb yield surface was treated by using a smooth hyperbolic approximation function [26] to treat the singularity at the apex and by using a trigonometric approximation to smooth the sharp corners in the meridional plane [27]. More recently, there has been work done to provide a smooth hyperbolic approximation to a generalized yield function, which combines the yield criteria of Tresca, Mohr-Coulomb, and Matsuoka-Nakai into a single expression, by a parameter for the inner rounding of the hexagonal Mohr-Coulomb in addition to the smoothing of the apex [28]. An additional method has been presented to combine multiple distinct yield functions into a single, general yield function that is both C^2 differentiable and convex [29]. Although model specific frameworks are usually more efficient, such as the work by Szwed and Kamińska [30] where they present a general form of the Drucker-Prager plastic potential, that is both smooth and convex, which can be calibrated based on experimental data and accounts for meridian slope changes.

The works mentioned previously only discuss the treatment of non-smooth yield surfaces in the forward analysis; however, in the context of gradient-based topology optimization, the evaluation of accurate gradient information is crucial for both the stress integration scheme and the sensitivity analysis. The use of other yield criterion, beyond the smooth von Mises, in topology optimization frameworks are primarily limited to the design of elastic structures subject to local stress constraints constructed by the specified yield function criterion [31–34]. Another approach in topology optimization consists of approximating the Drucker-Prager elastoplastic material behavior using a surrogate nonlinear elasticity model [35]. Although these former approaches are pervasive, they omit the critical elastoplastic analysis and fail to capture the true dissipative physics. Research that incorporates the Drucker-Prager elastoplastic analysis in the topology optimization statement includes, for example, Alberdi and Khandelwal [36], which admits to the non-differentiable flow potential at the apex but neglects to treat this singularity. In addition, Bogomolny and Amir [5] used the Drucker-Prager plasticity for the design of steel-reinforced concrete structures by proposing a material interpolation scheme which controls the influence of pressure in the yield function; hence allowing for the elastoplastic analysis of the two nonlinear material candidates. *To the best of the authors' knowledge, no topology optimization frameworks have been presented to address the gradient-discontinuity of the Drucker-Prager flow potential.*

In this work we establish a topology optimization framework which incorporates a Smooth Hyperbolic Drucker-Prager (SHDP) yield criterion in the elastoplastic analysis. The presented SHDP closely approximates the original non-smooth Drucker-Prager yield criterion, hence treating the singularity at the apex for valid sensitivity information while accurately representing the material behavior based on the original Drucker-Prager yield criterion. The topology optimization framework consists of an objective of maximizing the plastic work of the structure subject to a global volume constraint. In addition, the path dependent sensitivity analysis for the topology optimization framework is provided along with the return mapping algorithm derived for the SHDP elastoplastic analysis. The examples provided herein are based on the material properties of the Ti-6Al-4V titanium alloy [37] in an effort to obtain realistic engineering solutions based on the evidence supporting pressure dependence on metal plasticity. In addition, the titanium alloy obtains different yield stresses in compression and tension which provides secondary support for the use of the asymmetric yield criteria.

The remainder of this paper is organized as follows. In Section 2 we present the details of the original Drucker-Prager yield criteria along with the SHDP yield criteria. Section 3 provides information on the nonlinear finite element analysis and presents the equations describing the elastoplastic constitutive model. The section also describes the return mapping algorithm derived by the authors for the SHDP constitutive model along with a discussion on the update of the plastic multiplier increment and the deviatoric measure of stress by using the Bisection method. In Section 4 the details of the topology optimization formulation are shown and discussed. Section 5 provides an explanation on the path dependent sensitivity analysis procedure along with the explicit expressions for the partial derivatives. Finally, numerical results are presented in Section 6. Concluding remarks are made in Section 7 with additional information provided in the Appendices.

2. Drucker-Prager yield criterion: Original and smooth

Here we begin by describing the original Drucker-Prager yield criterion, while noting the gradient singularity at the apex of the yield surface. We then explain a Smooth Hyperbolic Drucker-Prager yield criterion which smoothly approximates the original. This smooth yield criterion is adopted in our constitutive model and used in our presented elastoplastic topology optimization framework.

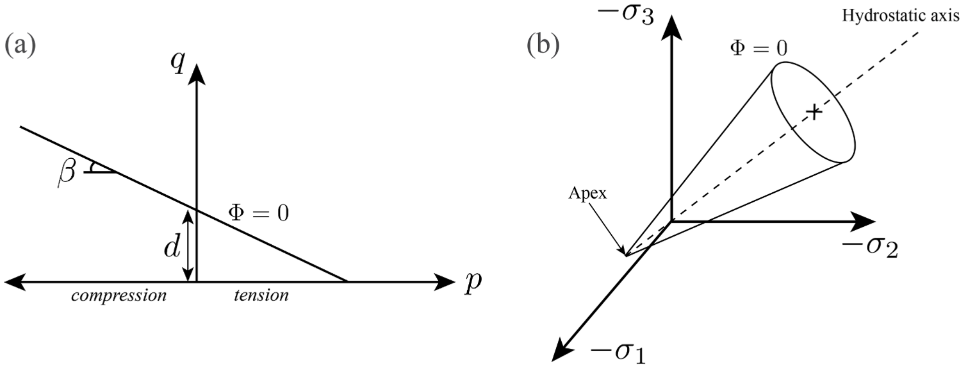

Fig. 1. Drucker-Prager yield function in (a) the $q - p$ axis and in (b) the principle stress space.

2.1. *Original Drucker-Prager*

We may describe the original Drucker-Prager yield criterion below [22] which is dependent on both the deviatoric, $\boldsymbol{s} = \mathbb{P}_{dev} : \boldsymbol{\sigma}$ and the pressure, $p = \frac{1}{3}\boldsymbol{I} : \boldsymbol{\sigma}$ components of the stress, $\sigma = p\boldsymbol{I} + \boldsymbol{s}$, where deviatoric projection tensor is defined by $\mathbb{P}^{dev} = \mathbb{I}^s - \frac{1}{3}\boldsymbol{I} \otimes \boldsymbol{I}$ with the fourth order symmetric identity tensor defined by $\mathbb{I}^s_{ijkl} = \frac{1}{2}\left(\delta_{ik}\delta_{jl} + \delta_{il}\delta_{jk}\right)$. The scalar measure of the deviatoric stress used in the yield function is defined by,

$$q = \sqrt{3/2} \cdot \|\boldsymbol{s}\|. \tag{1}$$

Additional terms are introduced to describe the asymmetric yielding behavior between the hydrostatic pressure under tension and compression with β denoting the friction angle, $\eta = \tan\beta$ representing the slope of the function in the $q - p$ axis, and d denoting the cohesion which represents the shear strength under zero normal stress [20].

$$\Phi(\boldsymbol{\sigma}) = q + \eta p - d = 0 \tag{2}$$

The cohesion may be determined by the compressive or the tensile yield strength of the material. We define the cohesion from the uniaxial compressive yield strength by [38]:

$$d = \left(1 - \frac{1}{3}\tan\beta\right)\sigma_c. \tag{3}$$

The Drucker-Prager yield function describes a linear relationship between the pressure and the yielding, as shown in Fig. 1 (a). Note for this work we use the convention that negative pressure is associated with compression and positive pressure with tension. When viewing this yield criterion in the principal stress space (see Fig. 1 (b)), the Drucker-Prager yield surface takes the shape of a cone where the apex is located on the hydrostatic axis with a stress state of pure triaxial tension at the pressure limit by, $(p, q) = (d/\eta, 0)$. The apex of the yield function is nondifferentiable, which impacts both the stress integration scheme for associative plastic flow and the sensitivity analysis in the topology optimization procedure. Hence, we address this by the smooth hyperbolic function.

2.2. *Smooth hyperbolic Drucker-Prager*

In this work, we adopt the smooth hyperbolic approximation function based off the work by Szwed [39]. The smooth approximation function is obtained by forming a quadratic equation from the original Drucker-Prager yield function by,

$$(q + \eta p - d)(-q + \eta p - d) = 0 \tag{4}$$

which is equivalent to,

$$\eta^2 p^2 - 2\, d\eta p - q^2 + d^2 = 0. \tag{5}$$

The pressure is obtained by finding the root of the quadratic expression. The root associated with the minus sign is the applicable choice for representing the Drucker-Prager yield criteria, leading to,

$$p = \frac{d}{\eta} - \sqrt{\left(\frac{q}{\eta}\right)^2}. \tag{6}$$

The square root term in Eq. (6) introduces nonlinearity to the function. To impose smoothness, we introduce a regularization term to modify this from a quadratic to hyperbolic form by,

$$p = \frac{d}{\eta} - \sqrt{\left(\frac{q}{\eta}\right)^2 + \left(\frac{\zeta}{\eta}\right)^2} \tag{7}$$

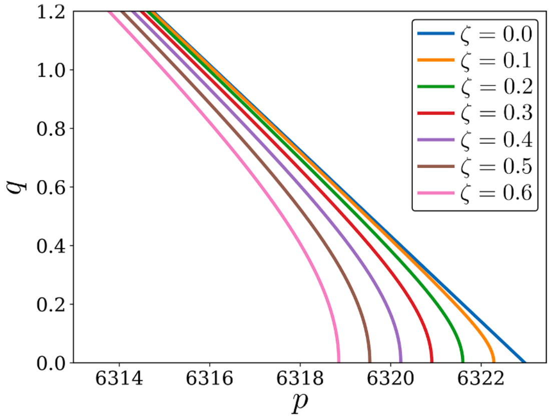

Fig. 2. Smooth approximation of the linear Drucker-Prager ($p-q$ space) for various regularization parameters, ζ.

where the regularization parameter denoted by ζ, which more closely approximates the linear yield criterion as $\zeta \to 0$. We can then rearrange the equation to obtain the final SHDP yield function, Φ_S.

$$\boxed{\Phi_S = p - \frac{d}{\eta} + \sqrt{\left(\frac{q}{\eta}\right)^2 + \left(\frac{\zeta}{\eta}\right)^2} = 0} \tag{8}$$

Here the conditions: $\zeta > 0$, $\eta > 0$, $d \geq 0$ and $p \leq d/\eta$, must hold in order for the model to be valid with the original Drucker-Prager. In Fig. 2 the smooth approximation of the linear Drucker-Prager criterion is shown to treat the singularity at the apex and to approach the original Drucker-Prager yield criterion as $\zeta \to 0$.

3. Nonlinear finite element analysis

The governing equations describe the mechanics of our elastoplastic structure under static equilibrium, which are used to inform the optimization problem. The strong form of the initial boundary value problem, in the absence of body forces, can be written by the following.

$$\begin{aligned} &\nabla \cdot \boldsymbol{\sigma} = \mathbf{0} \quad \text{in } \Omega \\ &\boldsymbol{u} = \bar{\boldsymbol{u}}_D \quad \text{on } \tilde{\Gamma}_D \subseteq \Gamma \\ &\boldsymbol{u} = \mathbf{0} \quad \text{on } \Gamma_D \subseteq \Gamma \end{aligned} \tag{9}$$

The strong form states that the divergence, $\nabla \cdot$ of the Cauchy stress tensor, $\boldsymbol{\sigma}$ must be equal to zero in the closed boundary, Ω. In addition, the structure is subject to zero and nonzero Dirichlet boundary conditions on the domain partition of $\Gamma_D \subseteq \Gamma$ and $\tilde{\Gamma}_D \subseteq \Gamma$ respectively, where $\tilde{\Gamma}_D \cap \Gamma_D = \emptyset$. The design domain and boundary conditions of the solid body are shown in Fig. 3. Under the assumption of small deformation, the total strain tensor may be computed by $\boldsymbol{\varepsilon} = \frac{1}{2}(\nabla \boldsymbol{u} + (\nabla \boldsymbol{u}^T))$ and is additively decomposed into its elastic and plastic counterparts by $\boldsymbol{\varepsilon} = \boldsymbol{\varepsilon}^e + \boldsymbol{\varepsilon}^p$. The pressure and deviatoric components of the stress may be written in terms of the elastic strain by, $p = \kappa \varepsilon^{vol}$ and $\boldsymbol{s} = 2G\mathbb{P}^{dev} : (\boldsymbol{\varepsilon}^e)$ where $\varepsilon^{vol} = Tr(\boldsymbol{\varepsilon}^e)$ and κ and G are the bulk and shear moduli, respectively. The moduli can be obtained from the elastic modulus, E and the Poisson's ratio, ν following the definitions $G = E/(2(1+\nu))$ and $\kappa = E/(3(1-2\nu))$ for isotropic materials. For this work we only consider problems of plane strain. For more information on the update of the plastic strain tensor for the SHDP constitutive model see Section 3.2.

3.1. Finite element analysis

The boundary value problem is solved by a numerical approximation of the strong form via the standard Galerkin finite element method in which the update to the global residual contribution from a single element, e can be defined by,

$$\boldsymbol{R}^e_{i+1} = \boldsymbol{f}^e_{int} = \int_{\Omega_e} \boldsymbol{B}^{u^T} : \boldsymbol{\sigma}_{i+1} dV \tag{10}$$

where $\boldsymbol{B}^u$ represents the matrix of shape function gradients and Ω_e the domain of the element. The global contribution of the Jacobian matrix for a single element may be expressed by,

$$\boldsymbol{J}^e_{i+1} = \frac{\partial \boldsymbol{R}^e_{i+1}}{\partial \bar{\boldsymbol{u}}_{i+1}}. \tag{11}$$

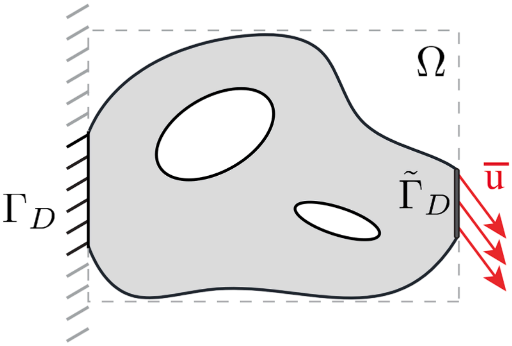

Fig. 3. The solid body design domain in the closed boundary, Ω, with an applied displacement, $\bar{\boldsymbol{u}}$, and Dirichlet boundary conditions, Γ_d and $\tilde{\Gamma}_D$, on the domain partition shown.

Here we would like to remark that the derivation of the consistent tangent from the presented return mapping algorithm is a nontrivial task; thus we instead compute the consistent tangent by taking the derivative of our global residual vector with respect to the vector of nodal displacements as indicated in Section 5.

Following the standard finite element procedure the element residual and Jacobian are assembled into their global counterpart.

$$\begin{aligned} \boldsymbol{R}_{i+1} &= \mathop{\mathcal{A}}_{e=1}^{N_{elem}} \boldsymbol{R}^e_{i+1} \\ \boldsymbol{J}_{i+1} &= \mathop{\mathcal{A}}_{e=1}^{N_{elem}} \boldsymbol{J}^e_{i+1} \end{aligned} \tag{12}$$

The Newton Raphson method is used to solve the nonlinear system of equations, updating the nodal displacement vector, $\bar{\boldsymbol{u}}_{i+1}$ by

$$\bar{\boldsymbol{u}}^{m+1}_{i+1} = \bar{\boldsymbol{u}}^{m}_{i+1} - \boldsymbol{J}^{m^{-1}}_{i+1} \boldsymbol{R}^{m}_{i+1} \tag{13}$$

where m is the iteration index. For this work we use the Newton Raphson method coupled with an inexact line search strategy.

3.2. Elastoplastic constitutive model

For the SHDP plasticity, we arrive at the following yield function as formerly described in Section 2,

$$\Phi_S(p,q) = p - \frac{d}{\eta} + \sqrt{\left(\frac{q}{\eta}\right)^2 + \left(\frac{\zeta}{\eta}\right)^2} = 0 \tag{14}$$

where the yielding is dependent on both the pressure and deviatoric components of the stress. Per definition of associative plastic flow, we set the flow potential to be equivalent to the yield function, $\Psi = \Phi$. Thus, we arrive at the flow rule defined by,

$$\boxed{\dot{\varepsilon}^p = \dot{\gamma}\frac{\partial \Phi}{\partial \boldsymbol{\sigma}} = \dot{\gamma}\boldsymbol{N}} \tag{15}$$

where $\dot{\gamma}$ is the plastic multiplier and $\boldsymbol{N}$ is the direction of plastic flow. Additionally, Karush-Kuhn-Tucker (KKT) conditions are introduced to enforce admissible stress states and to impose that plastic flow occurs only when the stress is on the yield surface,

$$\boxed{\Phi \leq 0,\ \dot{\gamma} \geq 0,\ \dot{\gamma}\Phi = 0.} \tag{16}$$

Lastly the consistency condition, alternatively referred to as the persistency condition, is introduced to dictate that in the occurrence of plastic slip the stress state must persist on the yield surface [40].

$$\boxed{\dot{\gamma}\dot{\Phi} = 0} \tag{17}$$

The former expressions are used in conjunction to form the initial value problem which describes the progression of the material's internal state for the specified load path.

3.3. Return mapping algorithm

The solution of the initial boundary value problem is determined numerically following the backward Euler method which leads to discretized equations in terms of pseudo time steps $i = 1, \dots, n$ [19]. In this work the authors derive the return mapping algorithm for the SHDP constitutive model following the generalized return mapping procedure in the stress invariant space by Borja [41]. The update of the state variables for the pseudo-time step, $i+1$, begins by the assembly of the trial state variables:

$$\varepsilon^{p,trial}_{i+1} = \varepsilon^p_i \tag{18}$$

$$\boldsymbol{s}_{i+1}^{trial} = 2G\mathbb{P}^{dev}(\boldsymbol{\varepsilon}_{i+1}^{e,trial}) \tag{19}$$

$$p_{i+1}^{trial} = \kappa \varepsilon_{i+1}^{vol,trial} \tag{20}$$

$$\alpha_{i+1}^{trial} = \alpha_i. \tag{21}$$

From this information the trial yield function, $\Phi_{S,i+1}^{trial}(q_{i+1}^{trial}, p_{i+1}^{trial})$, is computed. If the trial state is admissible ($\Phi_{S,i+1}^{trial} \leq 0$) we will update the state variables undergoing *elastic* loading by:

$$\boldsymbol{\varepsilon}_{i+1}^{p} = \boldsymbol{\varepsilon}_{i+1}^{p,trial} \tag{22}$$

$$\boldsymbol{s}_{i+1} = \boldsymbol{s}_{i+1}^{trial} \tag{23}$$

$$p_{i+1} = p_{i+1}^{trial} \tag{24}$$

$$\alpha_{i+1} = \alpha_{i+1}^{trial}. \tag{25}$$

For an inadmissible trial state ($\Phi_{S,i+1}^{trial} > 0$), the update of the state variables undergoing *plastic* loading is the following.

$$\boldsymbol{\varepsilon}_{i+1}^{p} = \boldsymbol{\varepsilon}_{i+1}^{p,trial} + \Delta\gamma_{i+1}\left(\frac{1}{3}\boldsymbol{I} + \sqrt{\frac{3}{2}}\frac{q_{i+1}^{trial}}{\eta^2}\frac{\boldsymbol{s}_{i+1}^{trial}}{\|\boldsymbol{s}_{i+1}^{trial}\|}\left(\left(\frac{q_{i+1}^{trial}}{\eta}\right)^2 + \left(\frac{\zeta}{\eta}\right)^2\right)^{-1/2}\right) \tag{26}$$

$$\boldsymbol{s}_{i+1} = \boldsymbol{s}_{i+1}^{trial} - 2\,G\Delta\gamma_{i+1}\sqrt{\frac{3}{2}}\frac{q_{i+1}^{trial}}{\eta^2}\frac{\boldsymbol{s}_{i+1}^{trial}}{\|\boldsymbol{s}_{i+1}^{trial}\|}\left(\left(\frac{q_{i+1}^{trial}}{\eta}\right)^2 + \left(\frac{\zeta}{\eta}\right)^2\right)^{-1/2} \tag{27}$$

$$p_{i+1} = p_{i+1}^{trial} - \kappa\Delta\gamma_{i+1} \tag{28}$$

The update for the accumulated plastic strain is defined by the following [38],

$$\alpha_{i+1} = \alpha_i + \frac{\boldsymbol{\sigma}_{i+1} : \dot{\boldsymbol{\varepsilon}}_{i+1}^{p}}{\sigma_c}. \tag{29}$$

An additional feature for the proposed return mapping algorithm is the update of the plastic multiplier increment. In this framework there no longer exists a closed form solution for the update of this plastic multiplier increment that satisfies $\Phi_{S,i+1}^{trial}(\Delta\gamma) = 0$. Hence we update the plastic multiplier increment by solving the following system of equations for the unknown variables, q_{i+1} and $\Delta\gamma_{i+1}$.

$$0 = q_{i+1} - q_{i+1}^{trial} + 3G\Delta\gamma_{i+1}\frac{q_{i+1}^{trial}}{\eta^2}\left(\left(\frac{q_{i+1}^{trial}}{\eta}\right)^2 + \left(\frac{\zeta}{\eta}\right)^2\right)^{-1/2} \tag{30}$$

$$0 = \underbrace{p_{i+1}^{trial} - \kappa\Delta\gamma_{i+1}}_{p_{i+1}} - \frac{d}{\eta} + \sqrt{\left(\frac{q_{i+1}}{\eta}\right)^2 + \left(\frac{\zeta}{\eta}\right)^2} \tag{31}$$

The system of equations may be compactly reduced into a single expression, where the bisection method is used in determining the update q_{i+1} by,

$$0 = q_{i+1} - q_{i+1}^{trial} + \frac{3Gq_{i+1}}{\kappa\eta^2}\left(\left(\frac{q_{i+1}}{\eta}\right)^2 + \left(\frac{\zeta}{\eta}\right)^2\right)^{-1/2}\left(p_{i+1}^{trial} - \frac{d}{\eta} + \sqrt{\left(\frac{q_{i+1}}{\eta}\right)^2 + \left(\frac{\zeta}{\eta}\right)^2}\right). \tag{32}$$

Once this is determined the plastic multiplier increment is updated by the following.

$$\boxed{\Delta\gamma_{i+1} = \frac{1}{\kappa}\left(p_{i+1}^{trial} - \frac{d}{\eta} + \sqrt{\left(\frac{q_{i+1}}{\eta}\right)^2 + \left(\frac{\zeta}{\eta}\right)^2}\right)} \tag{33}$$

The equations describing the evolution of the internal variables may be compactly described via the local residual equations by the vector $\boldsymbol{H}_i^{e_q}$ where the term e_q represents each quadrature point index, q associated with element index, e. This local residual vector contains the expressions for the update of the accumulated plastic strain, the plastic multiplier increment, and the plastic strain.

For the case of *elastic* loading the local residual is expressed as,

$$\boldsymbol{H}_i^{e_q} = \begin{bmatrix} h_{i,1}^{e_q} \\ h_{i,2}^{e_q} \\ h_{i,3}^{e_q} \end{bmatrix} = \begin{bmatrix} \alpha_i - \alpha_{i-1} \\ \Delta\gamma_i \\ \boldsymbol{\varepsilon}_i^p - \boldsymbol{\varepsilon}_{i-1}^p \end{bmatrix} = \begin{bmatrix} 0 \\ 0 \\ \boldsymbol{0} \end{bmatrix} \tag{34}$$

Table 1
Material properties of Titanium Ti-6Al-4V.

E [MPa]	ν	σ_y^c [MPa]	β [degrees]
113,800.0	0.342	970.0	8.3

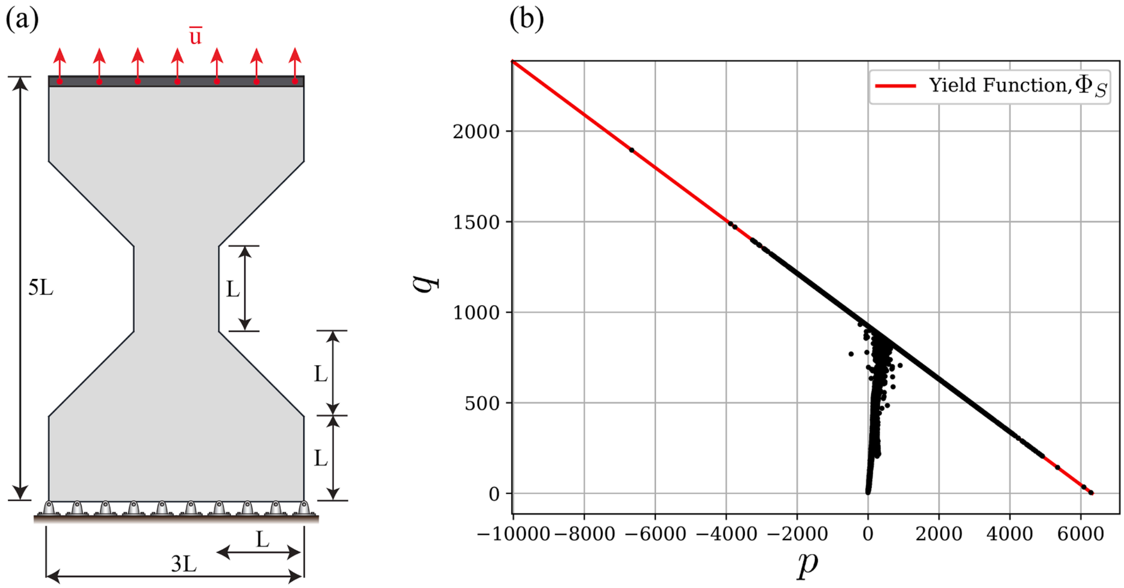

Fig. 4. The notched bar (a) domain and boundary conditions and (b) stress points for the forward analysis shown on the yield function.

and for *plastic* loading by,

$$\boldsymbol{H}_i^{e_q} = \begin{bmatrix} h_{i,1}^{e_q} \\ h_{i,2}^{e_q} \\ h_{i,3}^{e_q} \end{bmatrix} = \begin{bmatrix} \alpha_i - \alpha_{i-1} - \Delta\gamma_i \\ p_i - \frac{d}{\eta} + \sqrt{\left(\frac{q_i}{\eta}\right)^2 + \left(\frac{\zeta}{\eta}\right)^2} \\ \boldsymbol{\varepsilon}_i^p - \boldsymbol{\varepsilon}_{i-1}^p - \Delta\gamma_i \left(\frac{1}{3}\boldsymbol{I} + \sqrt{\frac{3}{2}}\,\frac{q}{\eta^2}\,\frac{\boldsymbol{s}}{\|\boldsymbol{s}\|}\left(\left(\frac{q}{\eta}\right)^2 + \left(\frac{\zeta}{\eta}\right)^2\right)^{-1/2}\right) \end{bmatrix} = \begin{bmatrix} 0 \\ 0 \\ \boldsymbol{0} \end{bmatrix}. \tag{35}$$

The elements in this work follow a polygonal element formulation, following the work by Talischi et al. [42]. For more information on the polygonal element quadrature rule adopted, see Alcazar et al. [43].

3.4. Notched bar in tension

Here we demonstrate the motivation for treating the singularity of the Drucker-Prager yield surface. First, we analyze a notched bar under tension in an SHDP forward analysis with material properties of the titanium alloy, Ti-6Al-4V [37] (see Table 1) with a cohesion, d computed based off of Eq. (3). Note that the angle of friction, β, is determined by interpolating between the tensile and compressive yield strength and that the regularization parameter, $\zeta = 0.6$. The regularization parameter of $\zeta = 0.6$ is selected for all numerical examples due to it begin well-conditioned, providing stability and convergence across all problems. The notched bar is subject to an applied displacement of $\bar{\boldsymbol{u}} = 4.792$ mm over 180 time steps with the geometry as presented in Fig. 4 (a) where the length, $L = 10$mm.

The SHDP forward analysis of the notched bar is performed with the final stress points plotted in Fig. 4 (b). The notched bar reaches the triaxial tension limit with stress points nearing or on the apex of the yield surface even under the small deformation assumption. For the same problem run without regularization ($\zeta = 0.0$), the forward problem fails to converge entirely. These results support the argument that the SHDP framework provides improved numerical stability and robustness in the solution of the forward analysis and subsequently in the topology optimization problem. Additionally, in topology optimization where the material domain is continuously changing, we argue that one will not know if a member of the structure will be subject to high triaxial tension a priori; thus, it is crucial to address the singularity of the yield function beforehand for valid sensitivity information at any stress state.

4. Topology optimization formulation

In this section we describe the details imposed on our topology optimization framework, beginning with the information on the material interpolation with specific emphasis on the plastic material interpolation. The details regarding the density filter and projection scheme are subsequently presented. Finally, the mathematical statement describing the topology optimization framework is provided.

4.1. Material interpolation

The problem setting is restricted to a relaxed continuous space of the element densities, $0 \leq \rho_e \leq 1$, to allow for the use of gradient-based optimizers. Intermediate densities often lack physical interpretation and thus a material interpolation scheme is implemented to influence densities to tend to either material ($\rho_e = 1$) or void ($\rho_e = 0$) by making intermediate densities mathematically inefficient to the optimizer. Here we use the Solid Isotropic Material Interpolation (SIMP) method [44] to interpolate the following material parameters.

$$E_e = \left(\epsilon_e + (1+\epsilon_e)\rho_e^{p_1}\right)E^{solid} \tag{36}$$

$$d_p = \left(\epsilon_p + (1+\epsilon_p)\rho_e^{p_2}\right)d^{solid} \tag{37}$$

In this work we separate the interpolation schemes for elastic and plastic material parameters [4]. For the elastic interpolation we denote the elastic ersatz parameter by $\epsilon_e = 10^{-8}$, the elastic penalization exponent by p_1, and the elastic modulus for the solid material by E^{solid}. The elastic material interpolation is equivalently imposed on the bulk modulus, κ and the shear modulus, G, components of the elastic modulus. For the plastic material interpolation the plastic penalization exponent is denoted by p_2 and the cohesion for the solid material is denoted by d^{solid}. The ersatz parameter for the plastic interpolation is computed such that the interpolated cohesion values for densities of zero never go below the regularization parameter ζ by setting $\epsilon_p = \zeta / d^{solid}$.

4.2. Density filter and projection scheme

In addition to the continuous parametrization of the densities we also impose the polynomial filter to address potential checkerboard issues. Following the work by Guest et al. [45], we use a polynomial filter based on the nodal design variables. The filter matrix, P_{ij}, is constructed from the filter radius, R and the coordinates, $\boldsymbol{x}$ of the nodes, i and j. This filter matrix is used to map the design variables, $\mathbf{z}$ to the filtered field, $\bar{\rho}$ by

$$\bar{\rho}_i = \frac{\mathrm{z}_j\ \omega(\boldsymbol{x}_i, \boldsymbol{x}_j)}{\sum_j \omega(\boldsymbol{x}_i, \boldsymbol{x}_j)} = P_{ij}\mathrm{z}_j \tag{38}$$

where

$$\omega(\boldsymbol{x}_i, \boldsymbol{x}_j) = \max\left(1 - \frac{\|\boldsymbol{x}_i - \boldsymbol{x}_j\|}{R},\ 0\right). \tag{39}$$

Once the filtered nodal design variables are computed, they are mapped onto the corresponding element centroid by the element shape functions. These filtered element design variables are then projected, as discussed below, to achieve the final physical densities.

The projection scheme is imposed in an effort to reduce intermediate densities in the transition region. The Heaviside projection scheme is prescribed on the filtered densities to achieve the final physical densities by

$$\rho_e(\bar{\rho}_e(\mathbf{z})) = \frac{\tanh(\beta\eta) + \tanh(\beta(\bar{\rho}_e - \eta))}{\tanh(\beta\eta) + \tanh(\beta(1-\eta))} \tag{40}$$

where the η controls the threshold at which the projection occurs and β governs the strength of the projection [46,47]. Information on the projection scheme continuation strategy is discussed in Section 6.

4.3. Topology optimization statement

For the intent of designing pressure-dependent elastoplastic structures with high energy absorption, we implement an objective function of maximizing plastic work. This function is dependent on the vector of design variables, $\boldsymbol{z}$ and the set of the nodal displacement vectors, $\boldsymbol{u}_i$ and the set of internal variables, $\boldsymbol{v}_i$ for all time steps, $i = 1, \ldots, n$. The computation of the plastic work is achieved through numerical integration where w_{e_q} is the Jacobian of the mapping multiplied by the Gauss quadrature weights, respectively. In this work we subject our structure to a global volume inequality constraint where the element densities, ρ_e and their corresponding element volume, v_e over the whole domain and total volume, V_{tot}, are bounded by the maximum volume fraction upper bound, $V_{\max}$. Additional equality constraints are imposed by $\boldsymbol{R}_i = \mathbf{0}$ and $\boldsymbol{H}_i = \mathbf{0}$, which ensures that the structure satisfies both the global and local equilibrium at every time step. Note that both the global and local residual vectors are dependent on the nodal displacement vector and internal variables information from the current and previous time step. The complete mathematical expression for the optimization statement is expressed below.

$$\boxed{\begin{aligned}
\max_{\mathbf{z}} \quad & f(\boldsymbol{\rho}(\mathbf{z}),\{\boldsymbol{u}_i\},\{\boldsymbol{v}_i\}) = \frac{1}{2}\sum_{i=1}^{n}\sum_{e=1}^{N_{elem}}\sum_{q=1}^{N_{quad}}\left(\boldsymbol{\sigma}_i^{e_q}+\boldsymbol{\sigma}_{i-1}^{e_q}\right):\left(\boldsymbol{\varepsilon}_i^{p,e_q}-\boldsymbol{\varepsilon}_{i-1}^{p,e_q}\right)w^{e_q}\\
\text{s.t.} \quad & g(\boldsymbol{\rho}(\mathbf{z})) = \frac{1}{V_{total}}\sum_{e=1}^{N_{elem}}\rho_e v_e - V_{max} \le 0\\
& \boldsymbol{R}_i(\boldsymbol{\rho}(\mathbf{z}),\boldsymbol{u}_i,\boldsymbol{u}_{i-1},\boldsymbol{v}_i,\boldsymbol{v}_{i-1}) = 0, \quad i = 1,\dots,n\\
& \boldsymbol{H}_i(\boldsymbol{\rho}(\mathbf{z}),\boldsymbol{u}_i,\boldsymbol{u}_{i-1},\boldsymbol{v}_i,\boldsymbol{v}_{i-1}) = 0, \quad i = 1,\dots,n
\end{aligned}} \tag{41}$$

The vector of design variables is updated by the optimizer and used to determine the filtered and projected element densities, $\boldsymbol{\rho}(\bar{\boldsymbol{\rho}}(\boldsymbol{z}))$. It is important to note that if the applied displacement causes the system to stay in the elastic regime, the plastic work objective would be zero, thus, we need to ensure that the applied displacement causes some plasticity for the structure to be optimized. Alternatively, the objective function and respective sensitivities could easily be modified to describe an elastic work objective function, which would design elastoplastic structures with greater stiffness.

5. Path dependent sensitivity analysis

Here we discuss the algorithmic procedure that is utilized in computing the path dependent sensitivity analysis. To begin, we adopt the adjoint method where we begin by forming the augmented Lagrangian function $\hat{f}$ as follows,

$$\hat{f}(\boldsymbol{\rho},\{\boldsymbol{u}_n\},\{\boldsymbol{v}_n\}) = f(\boldsymbol{\rho},\{\boldsymbol{u}_n\},\{\boldsymbol{v}_n\}) + \sum_{i=1}^{n}\left(\boldsymbol{\lambda}_i^T\boldsymbol{R}_i(\boldsymbol{\rho},\{\boldsymbol{u}_i\},\{\boldsymbol{u}_{i-1}\},\{\boldsymbol{v}_i\},\{\boldsymbol{v}_{i-1}\}) + \boldsymbol{\mu}_i^T\boldsymbol{H}_i(\boldsymbol{\rho},\{\boldsymbol{u}_i\},\{\boldsymbol{u}_{i-1}\},\{\boldsymbol{v}_i\},\{\boldsymbol{v}_{i-1}\})\right) \tag{42}$$

where f is the original objective function followed by the inner products of the local and global residuals $\boldsymbol{H}_i$ and $\boldsymbol{R}_i$ with their affiliated adjoint vectors $\boldsymbol{\lambda}_i$ and $\boldsymbol{\mu}_i$. Thus we proceed by obtaining the derivative of the augmented function with respect to the densities via the chain rule.

$$\begin{aligned}
\frac{d\hat{f}}{d\boldsymbol{\rho}} = \frac{df}{d\boldsymbol{\rho}} =& \frac{\partial f}{\partial\boldsymbol{\rho}} + \sum_{i=1}^{n}\frac{\partial f}{\partial\boldsymbol{u}_i}\frac{\partial\boldsymbol{u}_i}{\partial\boldsymbol{\rho}} + \frac{\partial f}{\partial\boldsymbol{v}_i}\frac{\partial\boldsymbol{v}_i}{\partial\boldsymbol{\rho}} + \sum_{i=1}^{n}\boldsymbol{\lambda}_i^T\left(\frac{\partial\boldsymbol{R}_i}{\partial\boldsymbol{\rho}} + \frac{\partial\boldsymbol{R}_i}{\partial\boldsymbol{u}_i}\frac{\partial\boldsymbol{u}_i}{\partial\boldsymbol{\rho}} + \frac{\partial\boldsymbol{R}_i}{\partial\boldsymbol{u}_{i-1}}\frac{\partial\boldsymbol{u}_{i-1}}{\partial\boldsymbol{\rho}} + \frac{\partial\boldsymbol{R}_i}{\partial\boldsymbol{v}_i}\frac{\partial\boldsymbol{v}_i}{\partial\boldsymbol{\rho}} + \frac{\partial\boldsymbol{R}_i}{\partial\boldsymbol{v}_{i-1}}\frac{\partial\boldsymbol{v}_{i-1}}{\partial\boldsymbol{\rho}}\right)\\
&+ \sum_{i=1}^{n}\boldsymbol{\mu}_i^T\left(\frac{\partial\boldsymbol{H}_i}{\partial\boldsymbol{\rho}} + \frac{\partial\boldsymbol{H}_i}{\partial\boldsymbol{u}_i}\frac{\partial\boldsymbol{u}_i}{\partial\boldsymbol{\rho}} + \frac{\partial\boldsymbol{H}_i}{\partial\boldsymbol{u}_{i-1}}\frac{\partial\boldsymbol{u}_{i-1}}{\partial\boldsymbol{\rho}} + \frac{\partial\boldsymbol{H}_i}{\partial\boldsymbol{v}_i}\frac{\partial\boldsymbol{v}_i}{\partial\boldsymbol{\rho}} + \frac{\partial\boldsymbol{H}_i}{\partial\boldsymbol{v}_{i-1}}\frac{\partial\boldsymbol{v}_{i-1}}{\partial\boldsymbol{\rho}}\right)
\end{aligned} \tag{43}$$

The adjoint vectors are determined in a specific manner to avoid the expensive computation of the terms $\partial\boldsymbol{u}_i/\partial\boldsymbol{\rho}$ and $\partial\boldsymbol{v}_i/\partial\boldsymbol{\rho}$. This is achieved by rearranging the terms from the previous equation to arrive at

$$\begin{aligned}
\frac{d\hat{f}}{d\boldsymbol{\rho}} =& \frac{\partial f}{\partial\boldsymbol{\rho}} + \frac{\partial\boldsymbol{u}_n}{\partial\boldsymbol{\rho}}\left(\frac{\partial f}{\partial\boldsymbol{u}_n} + \boldsymbol{\lambda}_n^T\frac{\partial\boldsymbol{R}_n}{\partial\boldsymbol{u}_n} + \boldsymbol{\mu}_n^T\frac{\partial\boldsymbol{H}_n}{\partial\boldsymbol{u}_n}\right) + \frac{\partial\boldsymbol{v}_n}{\partial\boldsymbol{\rho}}\left(\frac{\partial f}{\partial\boldsymbol{v}_n} + \boldsymbol{\lambda}_n^T\frac{\partial\boldsymbol{R}_n}{\partial\boldsymbol{v}_n} + \boldsymbol{\mu}_n^T\frac{\partial\boldsymbol{H}_n}{\partial\boldsymbol{v}_n}\right)\\
&+ \sum_{i=1}^{n}\left(\boldsymbol{\lambda}_i^T\frac{\partial\boldsymbol{R}_i}{\partial\boldsymbol{\rho}} + \boldsymbol{\mu}_i^T\frac{\partial\boldsymbol{H}_i}{\partial\boldsymbol{\rho}}\right) + \sum_{i=1}^{n-1}\frac{\partial\boldsymbol{u}_i}{\partial\boldsymbol{\rho}}\left(\frac{\partial f}{\partial\boldsymbol{u}_i} + \boldsymbol{\lambda}_i^T\frac{\partial\boldsymbol{R}_i}{\partial\boldsymbol{u}_i} + \boldsymbol{\mu}_i^T\frac{\partial\boldsymbol{H}_i}{\partial\boldsymbol{u}_i} + \boldsymbol{\lambda}_{i+1}^T\frac{\partial\boldsymbol{R}_{i+1}}{\partial\boldsymbol{u}_i} + \boldsymbol{\mu}_{i+1}^T\frac{\partial\boldsymbol{H}_{i+1}}{\partial\boldsymbol{u}_i}\right)\\
&+ \sum_{i=1}^{n-1}\frac{\partial\boldsymbol{v}_i}{\partial\boldsymbol{\rho}}\left(\frac{\partial f}{\partial\boldsymbol{v}_i} + \boldsymbol{\lambda}_i^T\frac{\partial\boldsymbol{R}_i}{\partial\boldsymbol{v}_i} + \boldsymbol{\mu}_i^T\frac{\partial\boldsymbol{H}_i}{\partial\boldsymbol{v}_i} + \boldsymbol{\lambda}_{i+1}^T\frac{\partial\boldsymbol{R}_{i+1}}{\partial\boldsymbol{v}_i} + \boldsymbol{\mu}_{i+1}^T\frac{\partial\boldsymbol{H}_{i+1}}{\partial\boldsymbol{v}_i}\right),
\end{aligned} \tag{44}$$

where the local and global adjoint vectors are computed such that they satisfy the following system of equations. Beginning with the final time step $i = n$ we obtain

$$\text{n}^{th}\text{ time step}: \begin{cases} \boldsymbol{\lambda}_n^T\dfrac{\partial\boldsymbol{R}_n}{\partial\boldsymbol{u}_n} + \boldsymbol{\mu}_n^T\dfrac{\partial\boldsymbol{H}_n}{\partial\boldsymbol{u}_n} = -\dfrac{\partial f}{\partial\boldsymbol{u}_n}\\[2ex] \boldsymbol{\lambda}_n^T\dfrac{\partial\boldsymbol{R}_n}{\partial\boldsymbol{v}_n} + \boldsymbol{\mu}_n^T\dfrac{\partial\boldsymbol{H}_n}{\partial\boldsymbol{v}_n} = -\dfrac{\partial f}{\partial\boldsymbol{v}_n} \end{cases} \tag{45}$$

and for all previous time steps, $i = 1,\dots,n-1$, the adjoint vectors must satisfy:

$$\text{i}^{th}\text{ time step}: \begin{cases} \boldsymbol{\lambda}_i^T\dfrac{\partial\boldsymbol{R}_i}{\partial\boldsymbol{u}_i} + \boldsymbol{\mu}_i^T\dfrac{\partial\boldsymbol{H}_i}{\partial\boldsymbol{u}_i} = -\left(\dfrac{\partial f}{\partial\boldsymbol{u}_i} + \boldsymbol{\lambda}_{i+1}^T\dfrac{\partial\boldsymbol{R}_{i+1}}{\partial\boldsymbol{u}_i} + \boldsymbol{\mu}_{i+1}^T\dfrac{\partial\boldsymbol{H}_{i+1}}{\partial\boldsymbol{u}_i}\right)\\[2ex] \boldsymbol{\lambda}_i^T\dfrac{\partial\boldsymbol{R}_i}{\partial\boldsymbol{v}_i} + \boldsymbol{\mu}_i^T\dfrac{\partial\boldsymbol{H}_i}{\partial\boldsymbol{v}_i} = -\left(\dfrac{\partial f}{\partial\boldsymbol{v}_i} + \boldsymbol{\lambda}_{i+1}^T\dfrac{\partial\boldsymbol{R}_{i+1}}{\partial\boldsymbol{v}_i} + \boldsymbol{\mu}_{i+1}^T\dfrac{\partial\boldsymbol{H}_{i+1}}{\partial\boldsymbol{v}_i}\right). \end{cases} \tag{46}$$

Notice in Eq. (46) that the solution to the adjoint vectors at the current time step, $\boldsymbol{\lambda}_i$ and $\boldsymbol{\mu}_i$, are dependent on information from the future time step, thus indicating the path dependent nature of the sensitivity analysis. Therefore these systems of equations need to be solved recursively. The solution to these system of equations may be compactly described by a single system of equations encompassing all time steps by the following.

$$\underbrace{\left(\frac{\partial \boldsymbol{R}_i}{\partial \boldsymbol{u}_i} - \frac{\partial \boldsymbol{R}_i}{\partial \boldsymbol{v}_i}\frac{\partial \boldsymbol{H}_i^{-1}}{\partial \boldsymbol{v}_i}\frac{\partial \boldsymbol{H}_i}{\partial \boldsymbol{u}_i}\right)^T}_{\text{element jacobian transpose}} \boldsymbol{\lambda}_i = \boldsymbol{F}_i^u - \frac{\partial \boldsymbol{H}_i^T}{\partial \boldsymbol{u}_i}\frac{\partial \boldsymbol{H}_i^{-T}}{\partial \boldsymbol{v}_i}\boldsymbol{F}_i^v \tag{47}$$

$$\boldsymbol{\mu}_i = \frac{\partial \boldsymbol{H}_i^{-T}}{\partial \boldsymbol{v}_i}\left(\boldsymbol{F}_i^v - \frac{\partial \boldsymbol{R}_i^T}{\partial \boldsymbol{v}}\boldsymbol{\lambda}_i\right) \tag{48}$$

This is done by denoting the right hand sides of Eqs. (45) and (46) by $\boldsymbol{F}_i^u$ and $\boldsymbol{F}_i^v$. For more information on the algorithmic procedure followed to compute the path dependent sensitivity analysis see, Alcazar et al. [43]. Once the adjoint vectors are determined, the derivative of the augmented objective function may be updated by:

$$\frac{d\hat{f}}{d\boldsymbol{\rho}} = \frac{\partial f}{\partial \boldsymbol{\rho}} + \sum_{i=1}^{n}\left(\boldsymbol{\lambda}_i^T\frac{\partial \boldsymbol{R}_i}{\partial \boldsymbol{\rho}} + \boldsymbol{\mu}_i^T\frac{\partial \boldsymbol{H}_i}{\partial \boldsymbol{\rho}}\right). \tag{49}$$

The partial derivatives required for this recursive, path dependent procedure are listed below.

$$\text{For } f : \begin{cases} \dfrac{\partial f}{\partial \boldsymbol{\rho}} \\ \dfrac{\partial f}{\partial \boldsymbol{u}_i} \\ \dfrac{\partial f}{\partial \boldsymbol{v}_i} \end{cases}, \quad \text{for } \boldsymbol{R}_i : \begin{cases} \dfrac{\partial \boldsymbol{R}_i}{\partial \boldsymbol{\rho}} \\ \dfrac{\partial \boldsymbol{R}_i}{\partial \boldsymbol{u}_i} \\ \dfrac{\partial \boldsymbol{R}_i}{\partial \boldsymbol{u}_{i-1}} \\ \dfrac{\partial \boldsymbol{R}_i}{\partial \boldsymbol{v}_i} \\ \dfrac{\partial \boldsymbol{R}_i}{\partial \boldsymbol{v}_{i-1}} \end{cases}, \quad \text{for } \boldsymbol{H}_i : \begin{cases} \dfrac{\partial \boldsymbol{H}_i}{\partial \boldsymbol{\rho}} \\ \dfrac{\partial \boldsymbol{H}_i}{\partial \boldsymbol{u}_i} \\ \dfrac{\partial \boldsymbol{H}_i}{\partial \boldsymbol{u}_{i-1}} \\ \dfrac{\partial \boldsymbol{H}_i}{\partial \boldsymbol{v}_i} \\ \dfrac{\partial \boldsymbol{H}_i}{\partial \boldsymbol{v}_{i-1}} \end{cases} \tag{50}$$

For the sensitivity of the augmented objective function with respect to the design variables $\mathbf{z}$, it is necessary to apply the chain rule to the sensitivities computed with respect to the filtered and projected design variables.

$$\frac{\partial f}{\partial \mathbf{z}} = \frac{\partial f}{\partial \boldsymbol{\rho}}\frac{\partial \boldsymbol{\rho}}{\partial \bar{\boldsymbol{\rho}}}\frac{\partial \bar{\boldsymbol{\rho}}}{\partial \mathbf{z}} = \frac{\partial f}{\partial \boldsymbol{\rho}}\frac{\partial \boldsymbol{\rho}}{\partial \bar{\boldsymbol{\rho}}}\mathbf{P} \tag{51}$$

5.1. Local residual derivatives

Here we define the partial derivatives of the local residual vector previously described in Eqs. (34) and (35). In this work, we define the set of independent internal variables to be, $\boldsymbol{v}_i^{e_q} = \{\alpha_i^{e_q}, \Delta\gamma_i^{e_q}, \boldsymbol{\varepsilon}_i^{p,e_q}\}$. For the scenario of elastic loading we may define the partial derivative of the local residual vector with respect to the internal variables by the following.

$$\begin{gathered} \frac{\partial \boldsymbol{H}_i^{e_q}}{\partial \alpha_i^{e_q}} = \begin{bmatrix} 1 \\ 0 \\ \mathbf{0} \end{bmatrix}, \frac{\partial \boldsymbol{H}_i^{e_q}}{\partial \alpha_{i-1}^{e_q}} = \begin{bmatrix} -1 \\ 0 \\ \mathbf{0} \end{bmatrix}, \frac{\partial \boldsymbol{H}_i^{e_q}}{\partial \Delta\gamma_i^{e_q}} = \begin{bmatrix} 0 \\ 1 \\ \mathbf{0} \end{bmatrix}, \\ \frac{\partial \boldsymbol{H}_i^{e_q}}{\partial \Delta\gamma_{i-1}^{e_q}} = \begin{bmatrix} 0 \\ 0 \\ \mathbf{0} \end{bmatrix}, \frac{\partial \boldsymbol{H}_i^{e_q}}{\partial \boldsymbol{\varepsilon}_i^{p,e_q}} = \begin{bmatrix} \mathbf{0} \\ \mathbf{0} \\ \mathbb{I}^s \end{bmatrix}, \frac{\partial \boldsymbol{H}_i^{e_q}}{\partial \boldsymbol{\varepsilon}_{i-1}^{p,e_q}} = \begin{bmatrix} \mathbf{0} \\ \mathbf{0} \\ -\mathbb{I}^s \end{bmatrix} \end{gathered} \tag{52}$$

The partial derivatives of the local residual vector with respect to the element densities and the nodal displacement variables for the elastic loading are,

$$\frac{\partial \boldsymbol{H}_i^{e_q}}{\partial \rho_e} = \begin{bmatrix} 0 \\ 0 \\ \mathbf{0} \end{bmatrix}, \frac{\partial \boldsymbol{H}_i^{e_q}}{\partial \boldsymbol{u}_i^{e_q}} = \begin{bmatrix} \mathbf{0} \\ \mathbf{0} \\ \mathbf{0} \end{bmatrix}. \tag{53}$$

For the evaluation of the partial derivatives of the local residual in the plastic state, we begin with the derivatives with respect to the internal local variables at the previous time step,

$$\frac{\partial \boldsymbol{H}_i^{e_q}}{\partial \alpha_{i-1}^{e_q}} = \begin{bmatrix} -1 \\ 0 \\ \mathbf{0} \end{bmatrix}, \frac{\partial \boldsymbol{H}_i^{e_q}}{\partial \Delta\gamma_{i-1}^{e_q}} = \begin{bmatrix} 0 \\ 0 \\ \mathbf{0} \end{bmatrix}, \frac{\partial \boldsymbol{H}_i^{e_q}}{\partial \boldsymbol{\varepsilon}_{i-1}^{p,e_q}} = \begin{bmatrix} \mathbf{0} \\ \mathbf{0} \\ -\mathbb{I}^s \end{bmatrix}. \tag{54}$$

The local residual partial derivatives with respect to the internal local variables at the current time step are listed below,

$$\frac{\partial \boldsymbol{H}_i^{e_q}}{\partial \alpha_i^{e_q}} = \begin{bmatrix} 1 \\ 0 \\ \mathbf{0} \end{bmatrix}, \ \frac{\partial \boldsymbol{H}_i^{e_q}}{\partial \Delta\gamma_i^{e_q}} = \begin{bmatrix} -1 \\ 0 \\ -\frac{1}{3}\boldsymbol{I} - \sqrt{\frac{3}{2}}\frac{q_i^{e_q}}{\eta^2}\frac{\boldsymbol{s}_i^{e_q}}{\|\boldsymbol{s}_i^{e_q}\|}\left(\boldsymbol{D}_i\right)^{-1/2} \end{bmatrix} \tag{55}$$

where

$$\boldsymbol{D}_i = \left(\frac{q_i^{e_q}}{\eta}\right)^2 + \left(\frac{\zeta}{\eta}\right)^2. \tag{56}$$

The remaining partial derivatives of the local residual vector with respect to the current plastic strain is determined as the following.

$$\frac{\partial \boldsymbol{H}_i^{e_q}}{\partial \boldsymbol{\varepsilon}_i^{p,e_q}} = \begin{bmatrix} \mathbf{0} \\ -\kappa\boldsymbol{I} - \frac{2\,Gq_i^{e_q}}{\eta^2}\sqrt{\frac{3}{2}}\frac{\boldsymbol{s}_i^{e_q}}{\|\boldsymbol{s}_i^{e_q}\|}\left(\boldsymbol{D}_i\right)^{-1/2} \\ \mathbb{I}^s + \frac{\Delta\gamma_i G}{\eta^2}\left(\boldsymbol{D}_i\right)^{-1/2}\left(3\mathbb{P}^{dev} - \frac{9}{2\eta^2}\boldsymbol{s}_i^{e_q}\otimes\boldsymbol{s}_i^{e_q}\left(\boldsymbol{D}_i\right)^{-1}\right) \end{bmatrix} = \begin{bmatrix} \mathbf{0} \\ -\boldsymbol{A_i} \\ \mathbb{I}^s + \boldsymbol{C}_i \end{bmatrix} \tag{57}$$

The partial derivatives of the local residual vector with respect to the element densities and the nodal displacement variables for the plastic loading are,

$$\frac{\partial \boldsymbol{H}_i^{e_q}}{\partial \rho_e} = \begin{bmatrix} 0 \\ E_i \\ \mathbf{0} \end{bmatrix}, \ \frac{\partial \boldsymbol{H}_i^{e_q}}{\partial \boldsymbol{u}_i} = \begin{bmatrix} \mathbf{0} \\ \boldsymbol{A}_i : \boldsymbol{B}^u \\ -\boldsymbol{C}_i : \boldsymbol{B}^u \end{bmatrix} \tag{58}$$

where

$$E_i = \frac{\partial\kappa}{\partial\rho_e}\mathrm{Tr}(\boldsymbol{\varepsilon}_i^{e_q} - \boldsymbol{\varepsilon}_i^{p,e_q}) - \frac{1}{\eta}\frac{\partial d}{\partial\rho_e} + \frac{2q_i^{e_q}}{\eta^2}\sqrt{\frac{3}{2}}\left(\boldsymbol{D}_i\right)^{-1/2}\frac{\boldsymbol{s}_i^{e_q}}{\|\boldsymbol{s}_i^{e_q}\|}\left(\boldsymbol{\varepsilon}_i^{e_q} - \boldsymbol{\varepsilon}_i^{p,e_q}\right)\frac{\partial G}{\partial\rho_e}. \tag{59}$$

Note that the terms $\partial G/\partial\rho_e$, $\partial\kappa/\partial\rho_e$, and $\partial d/\partial\rho_e$ can be obtained explicitly using the material interpolation schemes defined in Eqs. (36) and (37). In both elastic and plastic loading the local residual vector is independent of the nodal displacement variables from the previous time step leading to, $\partial\boldsymbol{H}_i^{e_q}/\partial\boldsymbol{u}_{i-1}^{e_q} = \mathbf{0}$.

5.2. Global residual derivatives

The global residual is written by the following,

$$\boldsymbol{R}_e^i = \int_{\Omega_e}\boldsymbol{B}^{u^T} : \mathbb{C} : (\boldsymbol{\varepsilon}^i - \boldsymbol{\varepsilon}^{p,i})\,dV \tag{60}$$

or equivalently by

$$\boldsymbol{R}_e^i = \int_{\Omega_e}\boldsymbol{B}^{u^T} : \left(2\,G\mathbb{P}^{dev} + 3\kappa\mathbb{I}^{vol}\right) : (\boldsymbol{\varepsilon}^i - \boldsymbol{\varepsilon}^{p,i})\,dV. \tag{61}$$

The nonzero contribution of the partial derivatives are determined to be,

$$\frac{\partial\boldsymbol{R}_e^i}{\partial\boldsymbol{\varepsilon}^{p,i}} = -\int_{\Omega_e}\boldsymbol{B}^{u^T} : \mathbb{C}\,dV \tag{62}$$

$$\frac{\partial\boldsymbol{R}_e^i}{\partial\boldsymbol{u}^i} = \int_{\Omega_e}\boldsymbol{B}^{u^T} : \mathbb{C} : \boldsymbol{B}^{u^T}\,dV \tag{63}$$

$$\frac{\partial\boldsymbol{R}_e^i}{\partial\rho_e} = \int_{\Omega_e}\boldsymbol{B}^{u^T} : \left(2\frac{\partial G}{\partial\rho_e}\mathbb{P}^{dev} + 3\frac{\partial\kappa}{\partial\rho_e}\mathbb{I}^{vol}\right) : (\boldsymbol{\varepsilon}^i - \boldsymbol{\varepsilon}^{p,i})dV. \tag{64}$$

5.3. Plastic work derivatives

In evaluating the partial derivatives of the plastic work objective function, we begin by separating the terms associated with the final time step, n, and previous time steps, $i = 1,\ldots,n-1$.

$$f(\boldsymbol{\rho},\{\boldsymbol{u}_n\},\{\boldsymbol{v}_n\}) = \frac{1}{2}\int_{\Omega}\boldsymbol{\sigma}_n : (\varepsilon_n^p - \varepsilon_{n-1}^p)dV + \frac{1}{2}\sum_{i=1}^{n-1}\int_{\Omega}\boldsymbol{\sigma}_i : \left(\varepsilon_{i+1}^p - \varepsilon_{i-1}^p\right)dV \tag{65}$$

The partial derivative of the plastic work, with respect to the element densities, is determined to be,

$$\frac{\partial f}{\partial \rho_e} = \frac{1}{2}\int_{\Omega} \frac{\partial \boldsymbol{\sigma}_n}{\partial \rho_e} : \left(\boldsymbol{\varepsilon}^p_n - \boldsymbol{\varepsilon}^p_{n-1}\right) dV + \frac{1}{2}\sum_{i=1}^{n-1}\int_{\Omega} \frac{\partial \boldsymbol{\sigma}_i}{\partial \rho_e} : \left(\boldsymbol{\varepsilon}^p_{i+1} - \boldsymbol{\varepsilon}^p_{i-1}\right) dV \tag{66}$$

where

$$\frac{\partial \boldsymbol{\sigma}_i}{\partial \rho_e} = \frac{\partial \kappa}{\partial \rho_e}\mathrm{Tr}(\boldsymbol{\varepsilon}_i - \boldsymbol{\varepsilon}^p_i)\boldsymbol{I} + 2\frac{\partial G}{\partial \rho_e}\mathbb{P}^{dev} : \left(\boldsymbol{\varepsilon}_i - \boldsymbol{\varepsilon}^p_i\right). \tag{67}$$

The partials of the plastic work, $\partial f/\partial \boldsymbol{v}_i$ and $\partial f/\partial \boldsymbol{u}_i$ are separated into expressions for the final time step, n, and all previous time steps, $i = 1, \dots, n-1$. Note that the plastic work does not explicitly depend on the internal variables of the equivalent plastic strain nor the plastic multiplier thus resulting in,

$$\frac{\partial f}{\partial \alpha_i} = \frac{\partial f}{\partial \Delta\gamma_i} = 0. \tag{68}$$

The remaining partial derivatives of the plastic work for the final time step, $i = n$, are determined as,

$$\frac{\partial f}{\partial \boldsymbol{\varepsilon}^p_n} = \frac{1}{2}\int_{\Omega} \kappa \boldsymbol{I}\otimes\boldsymbol{I} : \left(-\boldsymbol{\varepsilon}^p_n + \boldsymbol{\varepsilon}^p_{n-1}\right) dV + \frac{1}{2}\int_{\Omega} 2G\mathbb{P}^{dev} : \left(-\boldsymbol{\varepsilon}^p_n + \boldsymbol{\varepsilon}^p_{n-1}\right) dV + \frac{1}{2}\int_{\Omega}\left(\boldsymbol{\sigma}_n + \boldsymbol{\sigma}_{n-1}\right) dV \tag{69}$$

$$\frac{\partial f}{\partial \boldsymbol{u}_n} = \frac{1}{2}\int_{\Omega_e} \kappa \boldsymbol{I}\otimes\boldsymbol{I} : \left(\boldsymbol{\varepsilon}^p_n - \boldsymbol{\varepsilon}^p_{n-1}\right) : \boldsymbol{B}^u dV + \frac{1}{2}\int_{\Omega_e} 2\,G\mathbb{P}^{dev} : \left(\boldsymbol{\varepsilon}^p_n - \boldsymbol{\varepsilon}^p_{n-1}\right) : \boldsymbol{B}^u dV \tag{70}$$

and for the previous time steps, $i = 1, ., n-1$, as

$$\frac{\partial f}{\partial \boldsymbol{\varepsilon}^p_i} = \frac{1}{2}\int_{\Omega} \kappa \boldsymbol{I}\otimes\boldsymbol{I} : \left(-\boldsymbol{\varepsilon}^p_{i+1} + \boldsymbol{\varepsilon}^p_{i-1}\right) dV + \frac{1}{2}\int_{\Omega} 2G\mathbb{P}^{dev} : \left(-\boldsymbol{\varepsilon}^p_{i+1} + \boldsymbol{\varepsilon}^p_{i-1}\right) dV - \frac{1}{2}\int_{\Omega}\left(\boldsymbol{\sigma}_{i+1} - \boldsymbol{\sigma}_{i-1}\right) dV \tag{71}$$

$$\frac{\partial f}{\partial \boldsymbol{u}_i} = \frac{1}{2}\int_{\Omega_e} \kappa \boldsymbol{I}\otimes\boldsymbol{I} : \left(\boldsymbol{\varepsilon}^p_{i+1} - \boldsymbol{\varepsilon}^p_{i-1}\right) : \boldsymbol{B}^u dV + \frac{1}{2}\int_{\Omega_e} 2\,G\mathbb{P}^{dev} : \left(\boldsymbol{\varepsilon}^p_{i+1} - \boldsymbol{\varepsilon}^p_{i-1}\right) : \boldsymbol{B}^u dV. \tag{72}$$

The verification of the sensitivity analysis implementation can be found in Appendix A.

6. Numerical results

Three numerical examples are presented where different structures are shown considering the SHDP elastoplastic framework. In all the examples, we employ a constant elastic penalization exponent of $p_1 = 3$ and a plastic penalization exponent of $p_2 = 2.5$. In addition a projection scheme is imposed for the first 100 optimization iteration with a threshold value of $\eta = 0.5$ and a strength of $\beta = \min(1.0, 2R/\tau)$, where τ is the largest edge length in the finite element mesh. A continuation scheme on the projection strength is imposed starting at the 100^{th} optimization iteration where the projection strength is set to increase by four equal increments for each subsequent 25 optimization iterations until it reaches a maximum projection strength of $\beta_{\max} = 2R/\tau$; similar to the approach based on da Silva et al. [48]. The material properties are set to match the material properties of the titanium alloy, Ti-6Al-4V, following Table 1, unless otherwise specified. The regularization parameter in the SHDP model is set to $\zeta = 0.6$ and the Method of Moving Asymptotes [49] is used to solve the optimization problem with a move limit of 0.5. The domains are meshed using a Python version of `Polymesher` [43,50] to allow for the meshing of curved domains. All numerical examples are run for a maximum of 250 optimization iterations. For the convergence plots and the projection strength histories, see Appendix B. Additional problem specific information can be found in the example descriptions below.

6.1. Corbel domain

In this first example, we aim to analyze the influence of the pressure dependent yielding in the design of the Corbel domain by comparing the results obtained by considering the von Mises (VM) constitutive model versus the presented SHDP, in the topology optimization problem. The Corbel has a design domain with dimensions of $L = 40$ mm and an applied displacement width of $d = 3.2$ mm as shown in Fig. 5 (a). The right end of the Corbel is subject to an applied displacement of $\bar{\boldsymbol{u}} = -1.0$ mm over 20 time steps. The domain has a mesh composed of 18,000 polygonal elements with a filter radius of $R = 5$ mm and a volume fraction upper bound of $V_{\max} = 0.4$. In addition a passive region is imposed near the applied displacement region with a size of $d \times w$ where $w = 8.0\tau$. The problem is run first considering the standard VM constitutive model under perfect plasticity (no hardening) and an associative flow rule, in which pressure has no influence on yielding as seen by the yield function,

$$\Phi_{VM} = \sqrt{\frac{3}{2}\boldsymbol{s} : \boldsymbol{s}} - \sigma_y \tag{73}$$

where the yield strength is set as the cohesion $\sigma_y = d$ for a direct comparison. For this constitutive model the yield strength is independent of whether the loading is in compression and tension which motivates our use of symmetry constraints about the x-axis for this case. Following this examination, the same domain is run using the presented SHDP framework which introduces pressure dependence on the yielding and asymmetry between the yield strength under compression and tension.

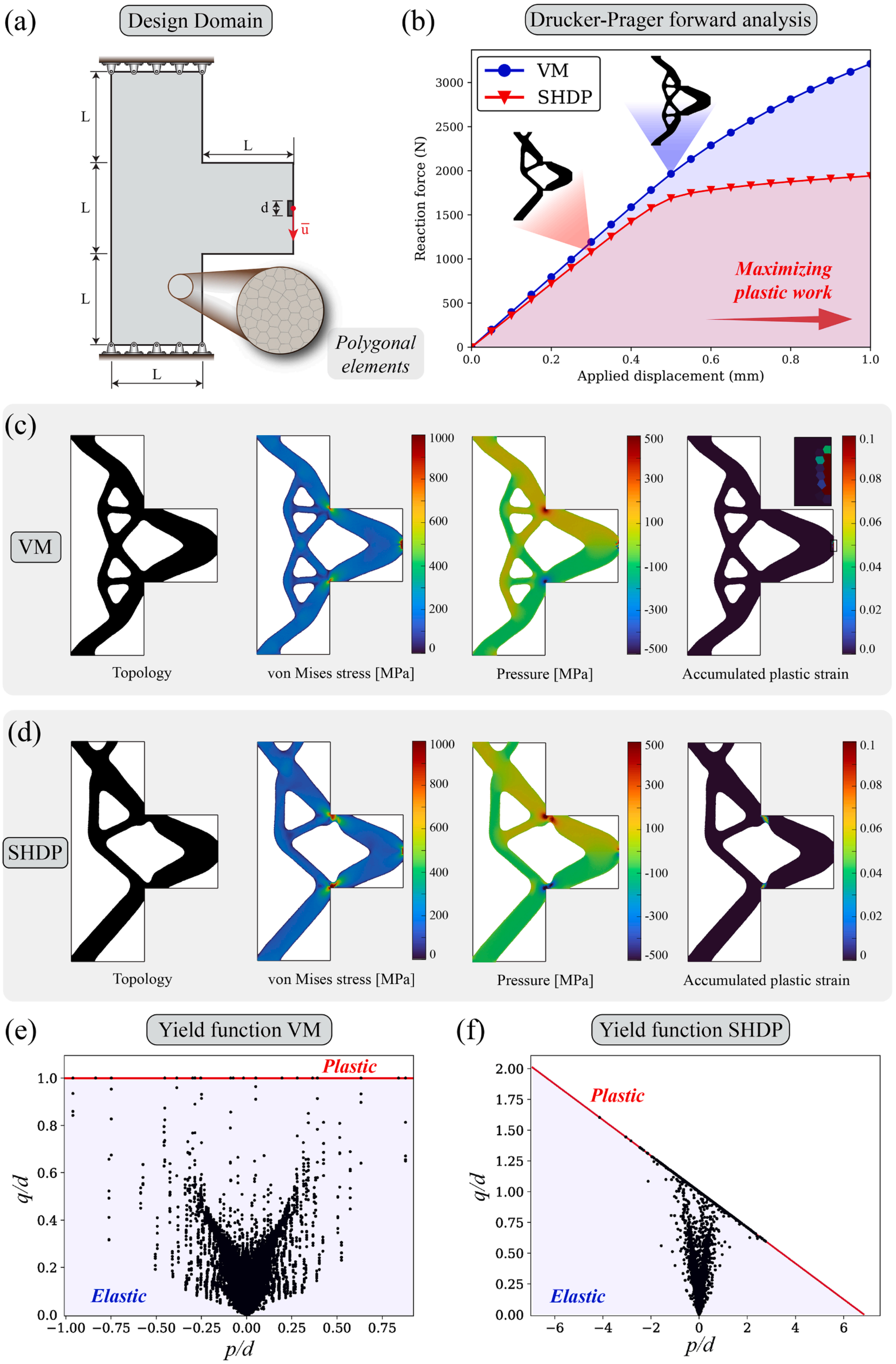

Fig. 5. The Corbel (a) design domain and boundary conditions; (b) Drucker-Prager forward analysis for the final topologies by the VM and SHDP; the results for the Corbel domain designed considering the (c) VM and the (d) SHDP constitutive model; the stress points on the normalized (e) VM and (f) SHDP yield function.

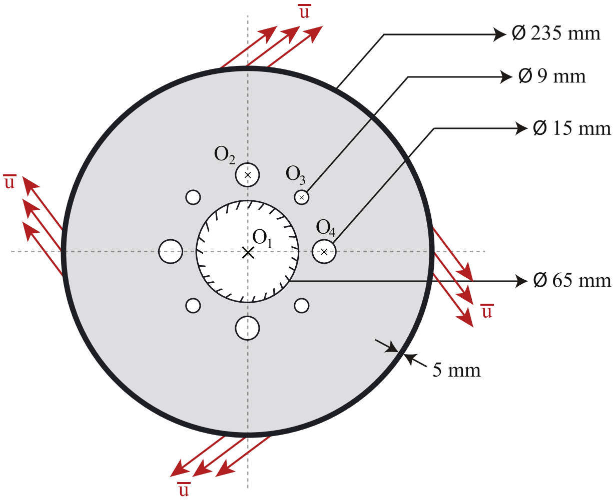

Fig. 6. Brake rotor domain and boundary conditions.

After obtaining the optimal topologies, one designed considering the SHDP and the other the VM, we extract the final topologies and perform a Drucker-Prager forward analysis as shown in Fig. 5 (b) to compare the performance of the two structures. From this analysis we observe that the SHDP topology leads to a less stiff structure with lower reaction forces throughout the displacement history compared to the VM structure, signifying a structure with high energy absorption. Additionally the plastic work of the SHDP structure is $\sim 82.15\,\%$ greater than the VM design with a plastic work of $W^p = 790.78$ N·mm compared to the VM topology with a plastic work of $W^p = 434.13$ N·mm. The aforementioned results indicate the importance of considering pressure-dependent yielding in the topology optimization framework when it is applicable to the material type (as motivated relevant for metal alloys in the introduction), because choosing the wrong constitutive model to represent your material can lead to significantly reduced design objective performance.

By observing the final topology obtained by optimizing the Corbel domain considering the VM constitutive model in Fig. 5 (c), we observe a high amount of von Mises stress in the reentrant corners and near the applied displacement region. In addition there exist a high amount of pressure in the reentrant corners, however, per the definition of the VM yield function, the pressure has no influence on the yielding and thus majority of the accumulated plastic strain is localized in the applied displacement region where the von Mises stress is the highest. For the structure obtained by the SHDP framework, as shown in Fig. 5 (d), we notice asymmetry of the topology with more material allocated to the members undergoing tension compared to compression due to the lower yield strength for tensile loading as consistent with the definition of the SHDP yield criteria. The final topology is also observed to have high amount of pressure and von Mises stress in the reentrant corners, however, in this case the pressure contributes to the yielding and thus we observe a large amount of accumulated plastic strain in the reentrant corners and greater plasticity in the SHDP versus the VM case.

The stress points are plotted on the normalized yield function at the final optimization step for both the VM and the SHDP in Fig. 5 (e-f), where the shaded blue area denotes stress points undergoing elastic loading and the stress points on the red line indicate that they are experiencing plastic loading. The normalized yield functions are obtained by dividing the material interpolated deviatoric and pressure components of the stress by the material interpolated cohesion such that the intercept is 1.0. For the VM yield function we see a rough symmetry of the stress points with the highest p/d value being less than 1.0. For the SHDP yield function it is observed that the highest p/d is around 3.0. This is due in part because the SHDP yield function has lower yield strength under tensile loading and that the objective function of plastic work may drive the structure to undergo more tensile loading to increase plasticity.

6.2. Brake rotor

Here we analyze a brake rotor domain subjected to multiple applied displacement regions. The curved domain is meshed for a total of $14,000$ unstructured polygonal elements. The dimensions and boundary conditions of the brake rotor domain are depicted in Fig. 6 and are set to match the dimensions of a standard AMC brake rotor [51]. The origins of the circles defining the disk domain are: $O_1 = (0.0\text{ mm}, 0.0\text{ mm})$, $O_2 = (0.0\text{ mm}, 48.75\text{ mm})$, $O_3 = (34.471\text{ mm}, 34.471\text{ mm})$, and $O_4 = (48.75\text{ mm}, 0.0\text{ mm})$, where the remainder can be determined from the x-y symmetry. Two cases of applied displacements are examined for the rotor domain with $|\bar{\boldsymbol{u}}_x| = 0.8$ mm and $|\bar{\boldsymbol{u}}_y| = 0.8$ mm over 14 pseudo time steps: (1) tension as depicted in Fig. 6 and (2) compression, the opposite direction to what is shown in Fig. 6. The applied displacements are subjected on regions with an arc length defined by an angular range of 10°. The examples are subject to a volume fraction upper bound of $V_{\max} = 0.35$ and obtain a passive region of elements on the circumference on the domain with a thickness of 5 mm. The polynomial filter in applied with a relative filter radius of $R_{rel} = 3.0\tau$ and symmetry constraints are imposed about the x and y axis.

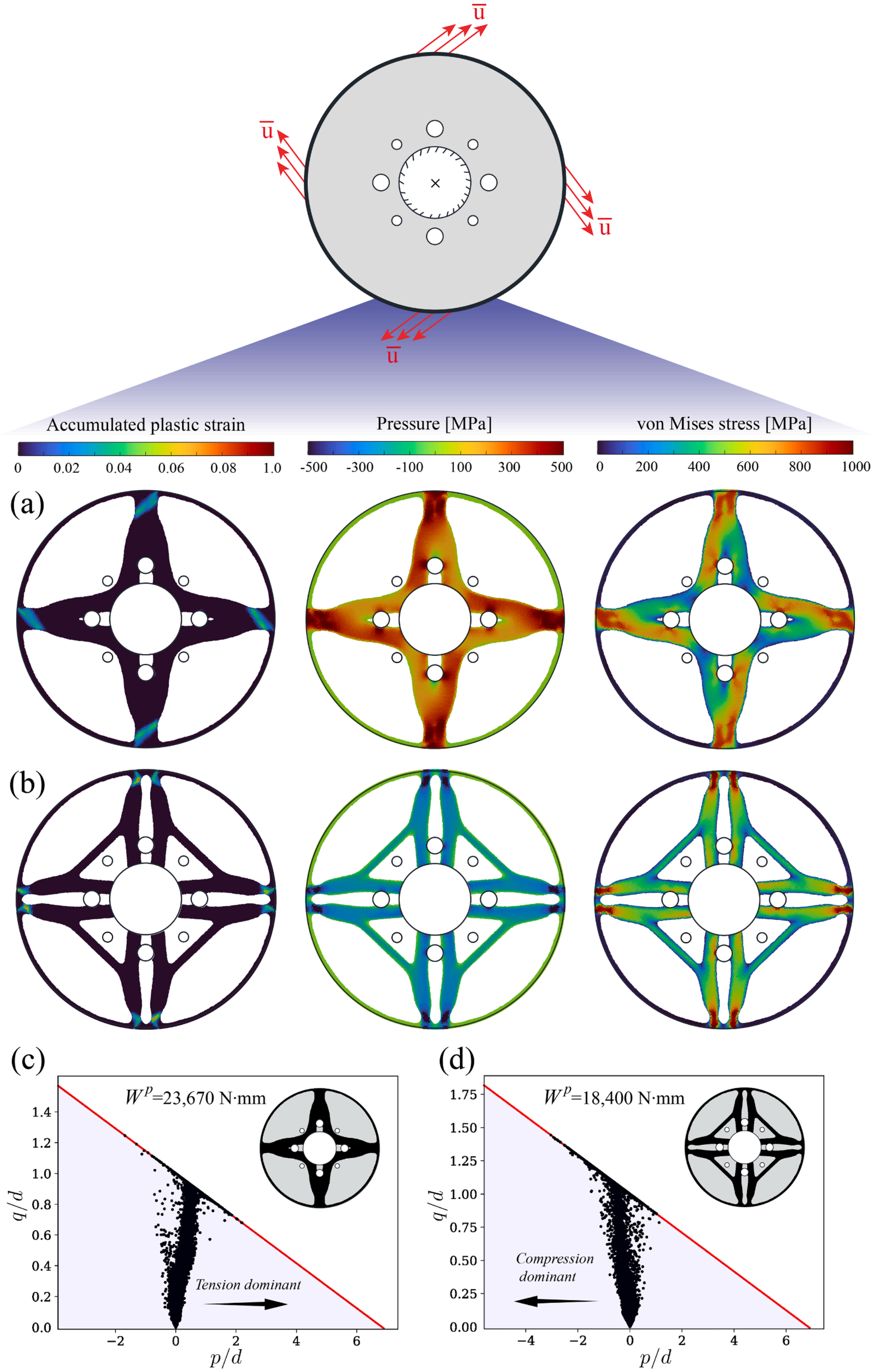

Fig. 7. The distribution of the accumulated plastic strain, pressure, and the von Mises stress for the brake rotor in (a) tension, (b) compression, and their associated normalized yield curves in (c) and (d), respectively.

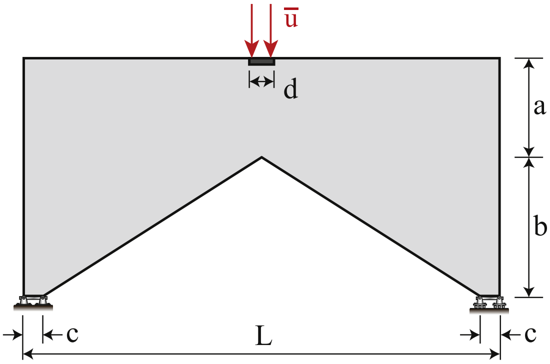

Fig. 8. Portal frame domain and boundary conditions.

In Fig. 7 we clearly see the significance that the asymmetric material behavior can have on the final optimized topology. For the same applied displacement magnitude we will obtain drastically different results whether the structure is undergoing tension or compression. In Fig. 7 (a) it is observed that the tension applied displacement will result in a cross type structure with high amounts of plastic strain forming a path from the applied displacement region inwards in the direction of the applied displacement. In the same locations, the structure obtains high amounts of pressure and von Mises stress as consistent with the definition of the Drucker-Prager yield function. For the rotor undergoing compression (see results in Fig. 7 (b)) the final topology splits around the four larger voids and has connecting members between the four main branches. The normalized yield functions for the rotors are depicted in Fig. 7 (c-d). The rotor experiencing tension obtains a higher final plastic work of $W^p = 23,670.0$ N·mm compared to the rotor undergoing compression with a final plastic work of $W^p = 18,400$ N·mm. This is because the structure will experience more plastic deformation for the same magnitude of applied displacement under tensile loading due to the lower yield strength in tension.

6.3. *Portal frame*

In this next example, we aim to analyze the influence of the friction angle β on the final topology. To begin, we analyze a Portal Frame with dimensions of $a = 12.5$ mm, $b = 17.5$ mm, $c = 2.75$ mm, $d = 4$ mm, and $L = 60$ mm as illustrated in Fig. 8. The Portal frame is discretized into a mesh of 16,000 polygonal elements and is subjected to a downward applied displacement of $\bar{u} = 1.0$ over 16 pseudo time steps. The volume fraction upper bound is defined to be $V_{\max} = 0.4$ and a relative filter radius of $R_{rel} = 3.0\tau$ is used. Three different cases are analyzed for different friction angles, one with the original friction angle, β_0, pertaining to the Titanium material properties specified in Table 1 and the other two with friction angles of $\beta = 0.05\beta_0$ and $\beta = 1.80\beta_0$. Note that for the friction angle of $\beta = 1.80\beta_0$, the problem is highly nonlinear since it is experiencing significantly more plasticity than the former problems due to the drastic decrease in the tensile yield strength. Thus for improved numerical stability and convergence in the forward problem, the pseudo time steps are increased to 60 steps in this case.

The final topologies for these three cases with their corresponding von Mises stress, pressure, and accumulated plastic strain distribution are illustrated in Fig. 9. The final plastic work objectives for the designs considering, $\beta = 0.05\beta_0$, $\beta = 1.0\beta_0$, and $\beta = 1.8\beta_0$ are $W^p = 443.0$ N·mm, $W^p = 444.2$ N·mm, and $W^p = 461.28$ N·mm, respectively. This demonstrates the impact of the increasing friction angle on the pressure dependent yielding and the increase of the total plastic work of the structure. In addition the normalized yield functions are depicted in Fig. 10 where we can directly observe the impact on the yield strength from increasing the friction angle. For the first case, where $\beta = 0.05\beta_0$, results in a roughly equal distribution of the stress points experiencing tensile or compressive loading due to the nearly symmetric yield surface (approaching the VM yield function as $\beta \to 0$). This is also corroborated by examining the final topology of this case, where the members undergoing both compression and tension have an equal distribution in size and shape. As the friction angle is increased from $\beta = \beta_0$ in the second case to $\beta = 1.8\beta_0$ in the final case, we notice higher amounts of accumulated plastic strain due to the lower yield strength under tensile loading. From these two cases we also notice a slight increase in the material distribution for members undergoing tension. In the final case, as shown on the right side of Fig. 10, it is observed that there exist many stress points breaching the apex of the yield surface, which provides justification and support for the presented treatment of the non-smooth Drucker-Prager model for the numerical stability of these stress states.

6.3.1. *Regularization parameter study*

In this next analysis we aim to analyze the influence on the regularization parameter, ζ and the impact of the smoothing the yield function. In this study the Half Portal frame domain with a friction angle of $\beta = 1.8\beta_0$ is examined from the previous numerical results. Here we study the problem for the nonsmooth case, without regularization, by $\zeta = 0.0$ and for smoothed cases of $\zeta = 0.1, 0.2, 0.4, 0.6$.

As summarized in Table 2, the case without regularization fails to converge from the first optimization iteration during the forward analysis. We also observe that if the regularization parameter is too small, as in the case of $\zeta = 0.1$, the problem may remain poorly conditioned due to steep or ill-scaled gradient information near the apex. Finally, the regularization parameters of $\zeta = 0.2$ and above are well conditioned providing numerical stability and convergence in the topology optimization problem. For the case of $\zeta = 0.2, 0.4, 0.6$ the final objective function values are 443.84 N·mm, 460.17 N·mm, and 461.28 N·mm, respectively. The influence of

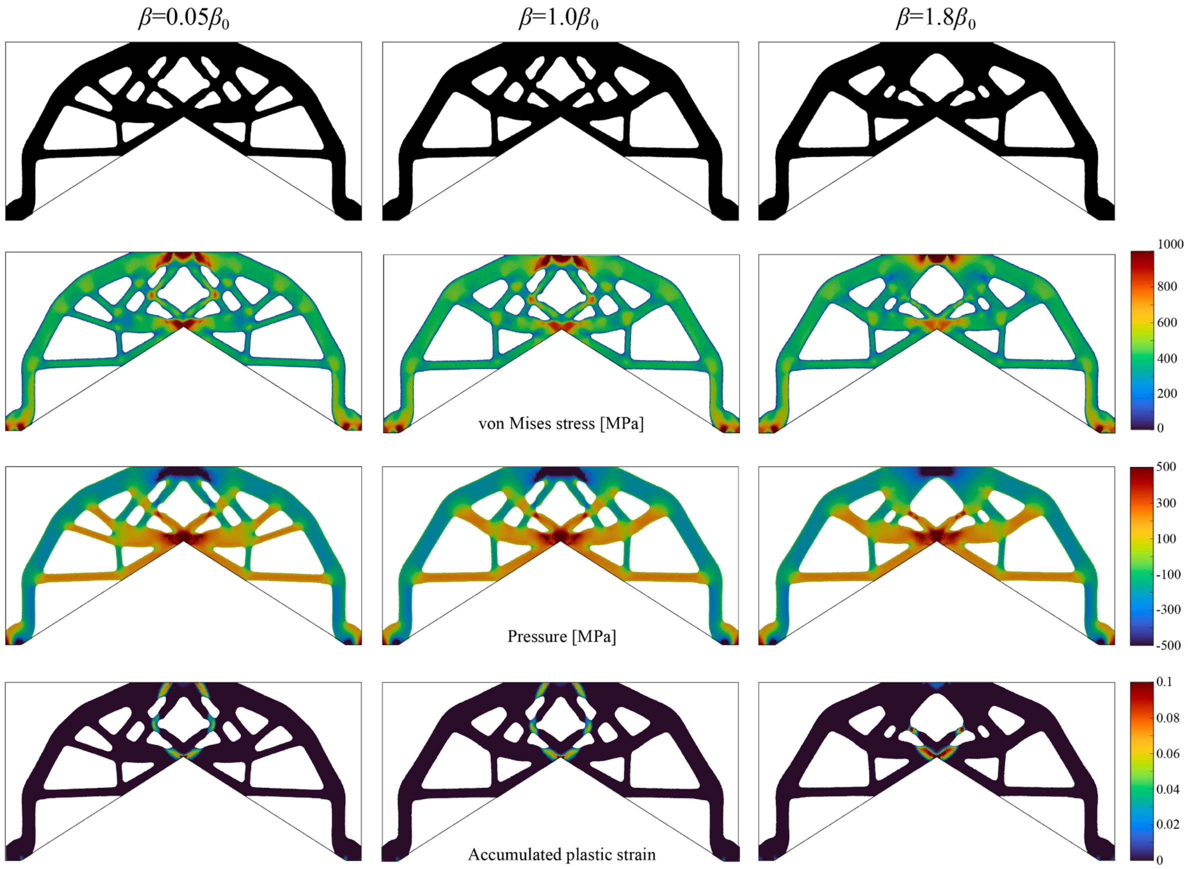

Fig. 9. Portal frame results with varying friction angles with cases, $\beta = 0.05\beta_0$ (left), $\beta = \beta_0$ (middle), and $\beta = 1.80\beta_0$ (right) with their corresponding von Mises stress, pressure, and accumulated plastic strain distribution.

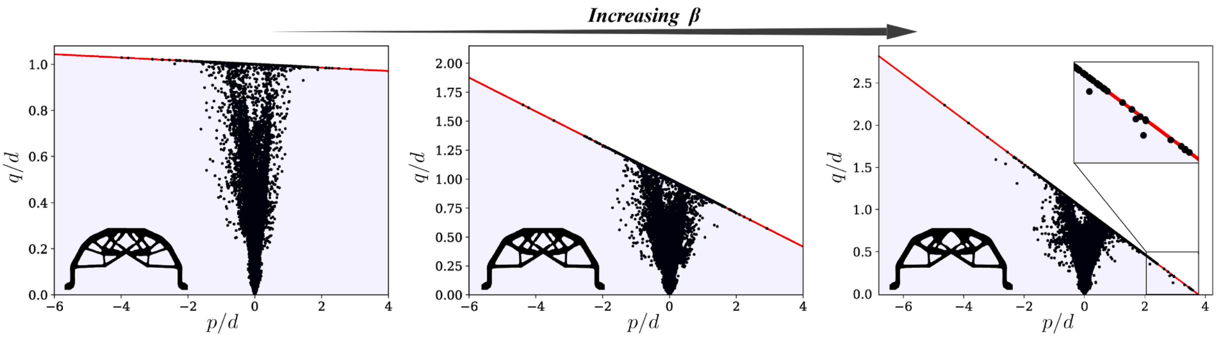

Fig. 10. Portal frame normalized yield surfaces for cases , $\beta = 0.05\beta_0$ (left), $\beta = \beta_0$ (middle), and $\beta = 1.80\beta_0$ (right).

Table 2
Regularization parameter study.

Regularization parameter, ζ	Convergence details
0.0 (no regularization)	Fails to converge in forward analysis in optimization iteration 1.
0.1	Fails to converge in forward analysis in optimization iteration 31.
0.2	Converges successfully.
0.4	Converges successfully.
0.6	Converges successfully.

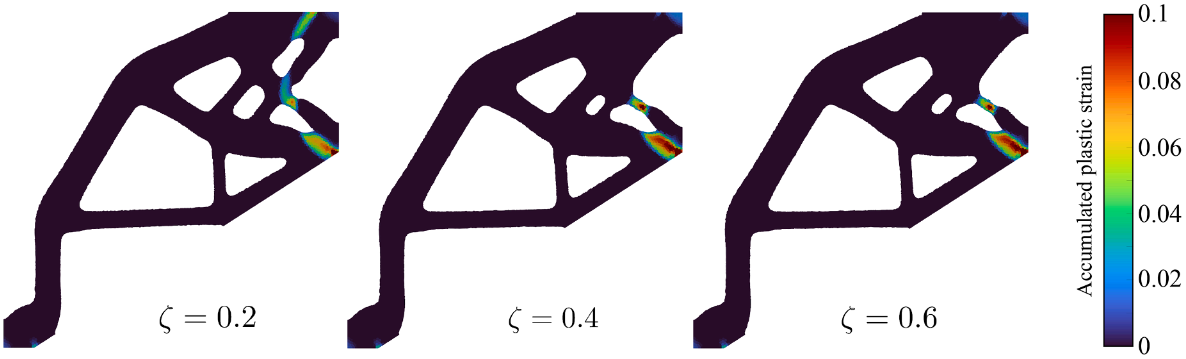

Fig. 11. Half Portal frame topology for three different cases of the regularization parameter; $\zeta = 0.2$ (left), $\zeta = 0.4$ (middle), and $\zeta = 0.6$ (right).

the regularization parameter on the topologies for these cases may be observed in Fig. 11. These results provide further justification on the practicality and usefulness of the proposed SHDP framework for improved numerical stability and in achieving results that could not have been achieved prior for the original nonsmooth yield function.

7. Conclusion

In this work we present a Smooth Hyperbolic Drucker-Prager (SHDP) topology optimization framework, which is proposed to treat the gradient discontinuity of the original Drucker-Prager yield surface at the apex; hence mitigating numerical instabilities for both the stress integration scheme and the gradient-based optimization problem. This includes a proposed return mapping algorithm based on the SHDP constitutive model with a discussion on the bisection method used for the update of the internal variables in the plastic loading state. We conduct the complete path dependent sensitivity analysis for the elastoplastic topology optimization framework composed by an objective function of maximizing plastic work subject to a global volume constraint. The results presented illustrate the influence of the Drucker-Prager material constitutive model on the final topology and the importance of considering the Drucker-Prager in the topology optimization framework when applicable in representing the design material. We place emphasis on the asymmetry of the yield surface and the effect of the pressure-dependent yielding. Most importantly, the results of the portal frame demonstrate that through the proposed SHDP framework we can achieve improved numerical stability for problems under high triaxial tension, which indicates the usefulness of this framework for achieving convergence in all stress states. The study on the regularization parameters also corroborates our claim of improved numerical stability by demonstrating that without regularization the problem fails to converge. The authors motivate the use of this framework for finite deformation kinematics where the stress points could more easily be subject to high triaxial tension on the apex - this is a potential future direction of this work.

Declarations

Conflict of interest The authors declare that they have no conflict of interest

Ethical approval The opinions presented in this article are those of the authors and do not necessarily reflect the views of the sponsoring organizations.

Replication of results To produce the results the authors refer the reader to the open source software `PolyPlas` provided by Alcazar et al. [43]. The program can be easily extended to consider the presented Smooth Hyperbolic Drucker-Prager framework from the details provided herein.

CRediT authorship contribution statement

Emily Alcazar: Writing – original draft, Visualization, Validation, Software, Methodology, Investigation, Formal analysis, Conceptualization; **Glaucio H. Paulino:** Writing – review & editing, Investigation, Conceptualization, Supervision, Resources, Project administration, Funding acquisition.

Data Availability

Data will be made available on request.

Declaration of competing interest

The authors declare they have no conflict of interests.

Acknowledgments

The authors would like to acknowledge the financial support provided by the National Science Foundation (NSF) Graduate Research Fellowship Program. In addition we would wish to extend our gratitude for the support granted by the Margareta Engman Augustine endowment at Princeton University. The authors would also like to extend their gratitude to Dr. Jonathan Russ for the many fruitful and insightful discussions pertaining to this work. Lastly we would like to acknowledge the support granted by the NSF from grants 2105811 and 2323415.

Appendix A. Sensitivity analysis verification

The cantilever beam example is provided here to verify that the sensitivity analysis is accurate. The cantilever is subject to a downward applied displacement of −0.2 mm over 16 time steps with the dimensions shown in Fig. A.1 (a). The material properties are following that of the titanium alloy, Ti-6Al-4v in Table 1. The cantilever has a random distribution of densities are shown in Fig. A.1 (b) with a structured finite element mesh composed of 400 elements. The numerical sensitivities are determined via the central finite difference method by,

$$\frac{d f(\boldsymbol{x})}{d x_i} \approx \frac{f(\boldsymbol{x}+\Delta\boldsymbol{x}_i) - f(\boldsymbol{x}-\Delta\boldsymbol{x}_i)}{2\Delta\boldsymbol{x}}. \tag{A.1}$$

The $\Delta\boldsymbol{x}_i$ represents a vector containing only the nonzero perturbation of 10^{-6} corresponding to design variable i. The comparison of the numerical sensitivities versus the analytical sensitivities obtained by the equations shown in Section 5 are shown in Fig. A.1 (c-d). The plots of the percent difference error provide confidence in the analytical sensitivities used.

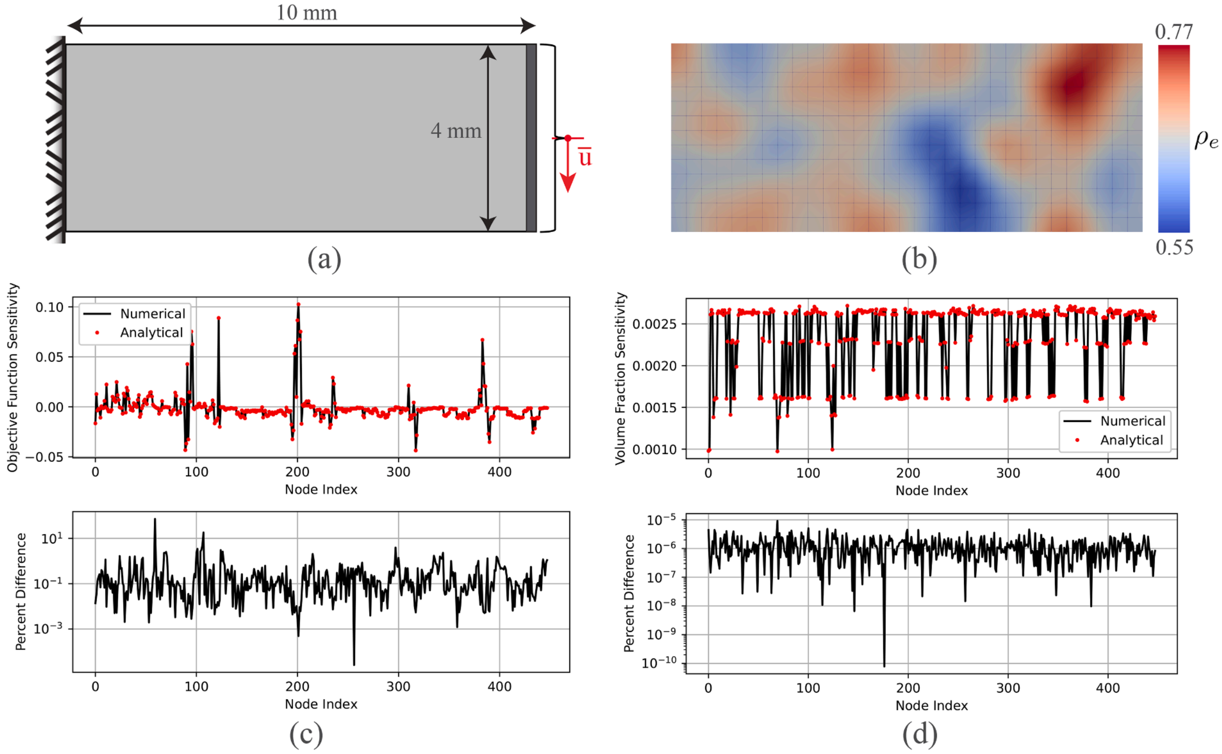

Fig. A.1. Finite difference sensitivity analysis verification of the (a) cantilever beam domain with (b) random density distribution and plots comparing the analytical sensitivities against the numerical sensitivities for (a) the plastic work objective function and (b) the volume fraction constraint.

Appendix B. Convergence plots

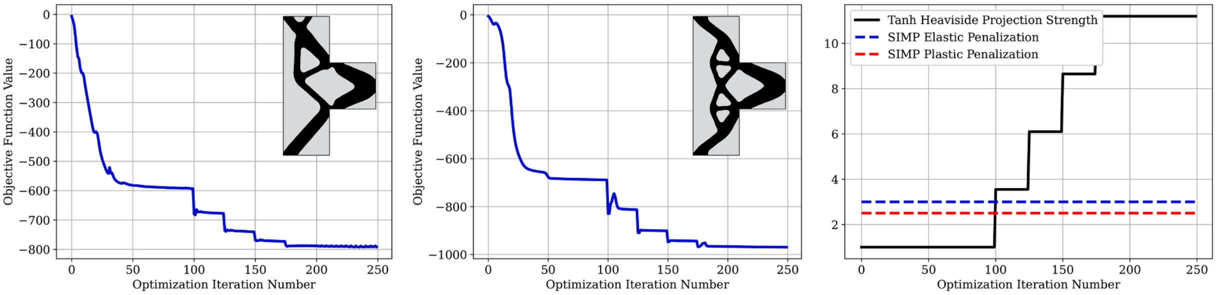

Fig. B.2. The convergence plots for the SHDP Corbel (left), the VM Corbel (middle), and the projection strength and material penalization information (right).

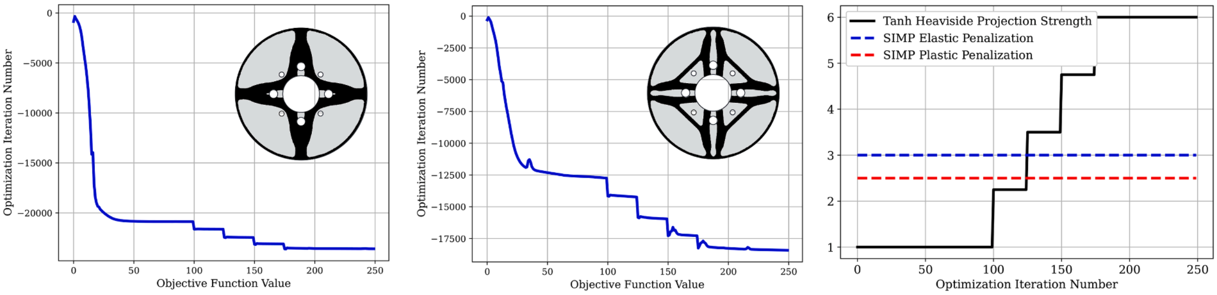

Fig. B.3. The convergence plots for the brake rotor example in tension (left), in compression (middle), and the projection strength and material penalization information (right).

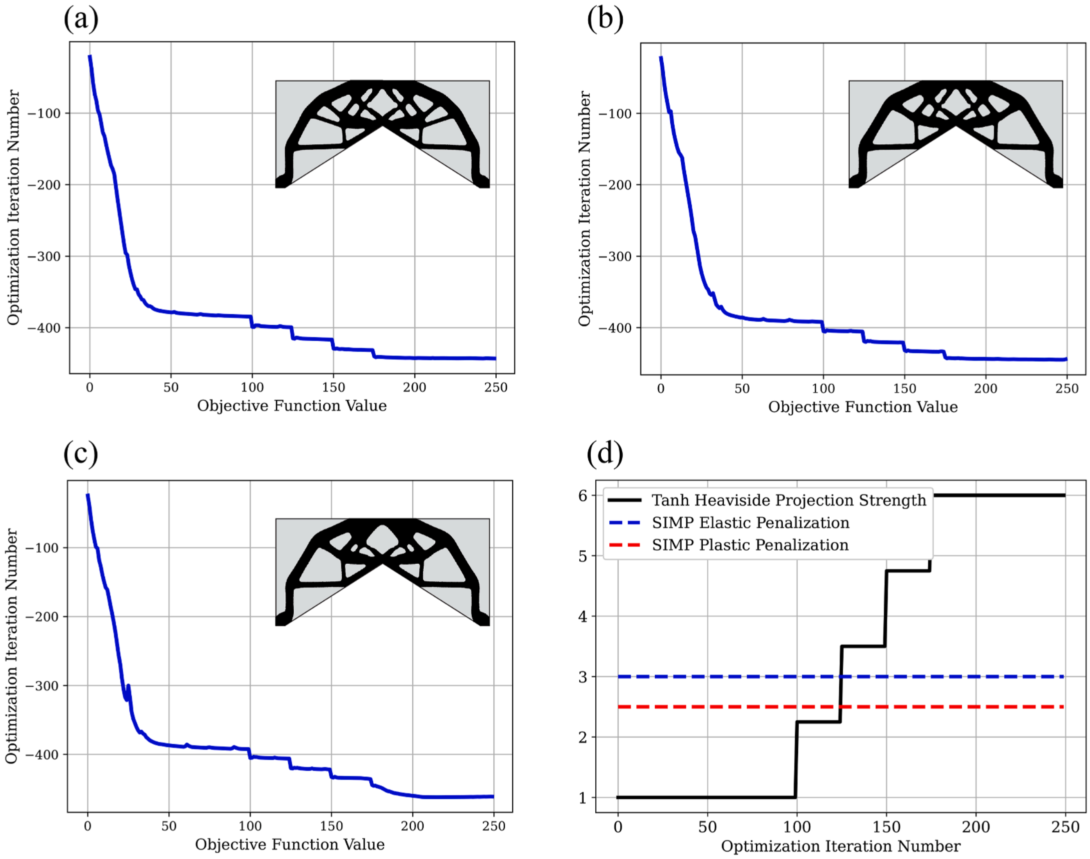

Fig. B.4. Half portal frame convergence for cases (a) $\beta = 0.05\beta_0$, (b) $\beta = \beta_0$, and (c) $\beta = 1.8\beta_0$; with the (d) projection strength and material penalization history.

References

[1] M.P. Bendsøe, N. Kikuchi, Generating optimal topologies in structural design using a homogenization method, Comput. Methods Appl. Mech. Eng. 71 (2) (1988) 197–224.
[2] G.I.N. Rozvany, A critical review of established methods of structural topology optimization, Struct. Multidiscip. Optim. 37 (2009) 217–237.
[3] J.D. Deaton, R.V. Grandhi, A survey of structural and multidisciplinary continuum topology optimization: post 2000, Struct. Multidiscip. Optim. 49 (2014) 1–38.
[4] K. Maute, S. Schwarz, E. Ramm, Adaptive topology optimization of elastoplastic structures, Struct. Optim. 15 (1998) 81–91.
[5] M. Bogomolny, O. Amir, Conceptual design of reinforced concrete structures using topology optimization with elastoplastic material modeling, Int. J. Numer. Methods Eng. 90 (13) (2012) 1578–1597.
[6] R. Alberdi, K. Khandelwal, Design of periodic elastoplastic energy dissipating microstructures, Struct. Multidiscip. Optim. 59 (2019) 461–483.
[7] J.B. Russ, H. Waisman, A novel elastoplastic topology optimization formulation for enhanced failure resistance via local ductile failure constraints and linear buckling analysis, Comput. Methods Appl. Mech. Eng. 373 (2021) 113478.
[8] J. Han, K. Furuta, T. Kondoh, S. Nishiwaki, K. Terada, Topology optimization of finite strain elastoplastic materials using continuous adjoint method: formulation, implementation, and applications, Comput. Methods Appl. Mech. Eng. 429 (2024) 117181.
[9] R.v. Mises, Mechanik der festen körper im plastisch-deformablen zustand, Nachrichten von der Gesellschaft der Wissenschaften zu Göttingen, Mathematisch-Physikalische Klasse 1913 (1913) 582–592.
[10] M. Wallin, V. Jönsson, E. Wingren, Topology optimization based on finite strain plasticity, Struct. Multidiscip. Optim. 54 (2016) 783–793.
[11] L. Li, G. Zhang, K. Khandelwal, Design of energy dissipating elastoplastic structures under cyclic loads using topology optimization, Struct. Multidiscip. Optim. 56 (2017) 391–412.
[12] L. Li, G. Zhang, K. Khandelwal, Failure resistant topology optimization of structures using nonlocal elastoplastic-damage model, Struct. Multidiscip. Optim. 58 (2018) 1589–1618.
[13] D.W. Abueidda, Z. Kang, S. Koric, K.A. James, I.M. Jasiuk, Topology optimization for three-dimensional elastoplastic architected materials using a path-dependent adjoint method, Int. J. Numer. Methods Eng. 122 (8) (2021) 1889–1910.
[14] N. Ivarsson, M. Wallin, O. Amir, D.A. Tortorelli, Plastic work constrained elastoplastic topology optimization, Int J Numer Methods Eng 122 (16) (2021) 4354–4377.
[15] E. Kuci, M. Jansen, Level set topology optimization of elasto-plastic materials with local stress constraints, Struct. Multidiscip. Optim. 65 (6) (2022) 170.
[16] G. Granlund, M. Wallin, Large-scale elasto-plastic topology optimization, Int. J. Numer. Methods Eng. (2024) 125e7583.
[17] Y. Jia, W. Li, X.S. Zhang, Multimaterial topology optimization of elastoplastic composite structures, J. Mech. Phys. Solids (2025) 196 106018.
[18] P.W. Bridgman, The effect of hydrostatic pressure on the fracture of brittle substances, J. Appl. Phys. 18 (2) (1947) 246–258.
[19] E.A. de Souza Neto, D. Peric, D.R.J. Owen, Computational Methods for Plasticity: Theory and Applications, John Wiley & Sons, 2011.
[20] J. Lubliner, Plasticity Theory, Courier Corporation, 2008.
[21] W.A. Spitzig, R.J. Sober, O. Richmond, The effect of hydrostatic pressure on the deformation behavior of maraging and HY-80 steels and its implications for plasticity theory, Metall. Trans. A 7 (1976) 1703–1710.

[22] D.C. Drucker, W. Prager, Soil mechanics and plastic analysis or limit design, Q. Appl. Math. 10 (2) (1952) 157–165.
[23] C.D. Wilson, A critical reexamination of classical metal plasticity, Journal Applied Mechanics 69 (1) (2002) 63–68.
[24] Y. Bai, T. Wierzbicki, A new model of metal plasticity and fracture with pressure and lode dependence, Int. J. Plast. 24 (6) (2008) 1071–1096.
[25] A.J. Abbo, S.W. Sloan, A smooth hyperbolic approximation to the mohr-Coulomb yield criterion, Comput. Struct. 54 (3) (1995) 427–441.
[26] O.C. Zienkiewicz, Some useful forms of isotropic yield surface for soil and rock mechanics, Finite Elements in Geomechanics edited by Gudehus, G. (1977) 179–190.
[27] S.W. Sloan, J.R. Booker, Removal of singularities in tresca and mohr–Coulomb yield functions, Commun. Appl. Numer. Methods 2 (2) (1986) 173–179.
[28] A.M. Lester, S.W. Sloan, A smooth hyperbolic approximation to the generalised classical yield function, including a true inner rounding of the Mohr-Coulomb deviatoric section, Comput. Geotech. 104 (2018) 331–357.
[29] A. Wilkins, B.W. Spencer, A. Jain, B. Gencturk, A method for smoothing multiple yield functions, Int J Numer Methods Eng 121 (3) (2020) 434–449.
[30] A. Szwed, I. Kamińska, A general form of Drucker-Prager type smooth and convex plastic potential. part 1: definition and features, in: MATEC Web of Conferences, 196, EDP Sciences, 2018, p. 01040.
[31] Y. Luo, Z. Kang, Topology optimization of continuum structures with Drucker–Prager yield stress constraints, Computers & Structures 90 (2012) 65–75.
[32] S. Amstutz, A.A. Novotny, E.A. de Souza Neto, Topological derivative-based topology optimization of structures subject to Drucker–Prager stress constraints, Comput. Methods Appl. Mech. Eng. 233 (2012) 123–136.
[33] O. Giraldo-Londoño, G.H. Paulino, A unified approach for topology optimization with local stress constraints considering various failure criteria: von Mises, Drucker–Prager, Tresca, Mohr–Coulomb, Bresler–Pister and Willam–Warnke, Proc. Royal Soc. A 476 (2238) (2020) 20190861.
[34] R.D. Kundu, W. Li, X.S. Zhang, Multimaterial stress-constrained topology optimization with multiple distinct yield criteria, Extreme Mech. Lett. 54 (2022) 101716.
[35] T. Zhao, E.N. Lages, A.S. Ramos, Jr, G.H. Paulino, Topology optimization considering the Drucker–Prager criterion with a surrogate nonlinear elastic constitutive model, Struct. Multidiscip. Optim. 62 (6) (2020) 3205–3227.
[36] R. Alberdi, K. Khandelwal, Topology optimization of pressure dependent elastoplastic energy absorbing structures with material damage constraints, Finite Elem. Anal. Des. 133 (2017) 42–61.
[37] ASM MatWeb, Material Property Data: MTP641, n.d., (https://asm.matweb.com/search/specificmaterial.asp?bassnum = mtp641). Accessed: 2025-01-12.
[38] D. Systèmes, SIMULIA User Assistance, 2022.
[39] A. Szwed, Dissipation function and elastoplastic constitutive relationships based on smooth Drucker–Prager yield condition, Theoretical Foundations of Civil Engineering 9 (2019) 95–105.
[40] J.C. Simo, T.J.R. Hughes, Computational Inelasticity, 7, Springer Science & Business Media, 2006.
[41] R.I. Borja, Plasticity, Springer-Verlag Berlin Heidelberg, 2013.
[42] C. Talischi, G.H. Paulino, A. Pereira, I.F.M. Menezes, Polytop: a matlab implementation of a general topology optimization framework using unstructured polygonal finite element meshes, Struct. Multidiscip. Optim. 45 (2012) 329–357.
[43] E. Alcazar, J.B. Russ, G.H. Paulino, PolyPlas: a Python implementation of a topology optimization framework for plasticity with unstructured polygonal finite elements, Struct. Multidiscip. Optim. 68 (8) (2025) 1–30.
[44] M.P. Bendsøe, Optimal shape design as a material distribution problem, Structural Optimization 1 (1989) 193–202.
[45] J.K. Guest, J.H. Prévost, T. Belytschko, Achieving minimum length scale in topology optimization using nodal design variables and projection functions, Int. J. Numer. Methods Eng. 61 (2) (2004) 238–254.
[46] S. Xu, Y. Cai, G. Cheng, Volume preserving nonlinear density filter based on heaviside functions, Struct. Multidiscip. Optim. 41 (2010) 495–505.
[47] F. Wang, B.S. Lazarov, O. Sigmund, On projection methods, convergence and robust formulations in topology optimization, Struct. Multidiscip. Optim. 43 (2011) 767–784.
[48] G.A. da Silva, A.T. Beck, O. Sigmund, Stress-constrained topology optimization considering uniform manufacturing uncertainties, Comput. Methods Appl. Mech. Eng. 344 (2019) 512–537.
[49] K. Svanberg, The method of moving asymptotes–a new method for structural optimization, Int. J. Numer. Methods Eng. 24 (2) (1987) 359–373.
[50] C. Talischi, G.H. Paulino, A. Pereira, I.F.M. Menezes, Polymesher: a general-purpose mesh generator for polygonal elements written in matlab, Struct. Multidiscip. Optim. 45 (2012) 309–328.
[51] M.A. Maleque, A.A. Adebisi, Q.H. Shah, Energy and cost analysis of weight reduction using composite brake rotor, Int. J. Veh. Struct. Syst. 4 (2) (2012) 69.